Results in Engineering 30 (2026) 110464

Contents lists available at ScienceDirect

Results in Engineering

journal homepage: www.sciencedirect.com/journal/results-in-engineering

Research paper

Using deep generative-based machine and ensemble learning framework for predicting ultimate bending capacity of circular steel tubes

Mahmood Sami Salah [a,1], Mohamed El Amine Ben Seghier [b,c,1,*], Sushant Gautam [d], Osama Ahmed Mohamed [e]

[a] Department of Built Environment, Oslo Metropolitan (OsloMet) University, Oslo, Norway
[b] Laboratory for Computational Mechanics, Institute for Computational Science and Artificial Intelligence, Van Lang University, Ho Chi Minh City, Vietnam
[c] Faculty of Mechanical, Electrical, and Computer Engineering, Van Lang School of Technology, Van Lang University, Ho Chi Minh City, Vietnam
[d] Simula Metropolitan, Oslo, 0167, Norway
[e] College of Engineering, Abu Dhabi University, Abu Dhabi, United Arab Emirates

ARTICLE INFO

Keywords:
Circular steel tubes
Ultimate bending capacity
Komogorov-Smirnov test
Copula generative adversarial networks synthesizer
Extreme gradient boosting
SHapley Additive exPlanations

ABSTRACT

Avoiding steel tubes from reaching their ultimate bending capacity is critical for civil and structural engineers in order to avoid substantial deformations that cause failures. However, conducting pure bending experimental tests on all types of steel tubes is a difficult task due to the associated high costs. This paper proposes a novel two-stage framework that combines deep generative learning, machine and ensemble learning models to accurately predict the ultimate bending capacity of circular steel tubes. In the first stage, the Copula Generative Adversarial Network is used to generate large synthetic databases of ultimate bending capacity for cold-formed and fabricated steel tubes based on limited experimental datasets, while the second stage uses various machine and ensemble learning models to accurately predict the ultimate bending capacity. The performance of each stage is examined using numerous numerical and graphical metrics, during the training, testing, and validation phases. Using the global performance indicator, the proposed Extreme Gradient Boosting model demonstrated the highest performance among the other models with *PI=0.7979* for fabricated circular tubes and *PI =0.8176* for cold-formed circular tubes, and coefficient of determination values of $R^2_{fabricated} = 0.9853$ and $R^2_{cold-formed} = 0.9663$, in the same respect. SHapley Additive exPlanations approach is then utilized to describe the best performing model behavior and the role of each variable in determining the ultimate bending capacity. The results of model explanation-based SHAP analysis revealed that steel tube thickness and diameter are the most influential variables in ultimate bending capacity predictions. The proposed framework indicates the importance of deep learning-based data generation in enhancing prediction outcomes in the situation of limited experimental results, as is the case of various materials science and engineering challenges.

1. Introduction

Circular steel tubes (CSTs) are widely utilized in the construction industry due to their exceptional structural properties comprising high strength-to-weight ratio, cost-effectiveness, and ease of fabrication [1, 2]. The closed cross-section of these structural elements provides superior resistance to torsional forces inducing particular suitability for applications requiring high stability and load-bearing efficiency [3]. Furthermore, CSTs have excellent energy dissipation capacity towards withstanding sever plastic deformation while preserving structural integrity [4]. In other words, CSTs are able to absorb large amounts of energy under pure bending conditions, which is essential for structures subjected to dynamic loading. These characteristics render CSTs for extensive use in large-span structures such as trusses, grid-systems, pipelines, nuclear power plants, and offshore platforms. Despite the structural advantages, CSTs are prone to buckling failure due to nonlinear behavior generated by the interaction of the external environment and circular tubes [5]. This arises from the material nonlinearities (e.g. steel transition into the plastic region), geometrical nonlinearities (e.g. large deformations that alter the tube's stability),

* Corresponding author.
E-mail address: benseghier@vlu.edu.vn (M.E.A. Ben Seghier).
[1] The first and second authors contributed equally to this work and share first authorship.

https://doi.org/10.1016/j.rineng.2026.110464
Received 20 May 2025; Received in revised form 19 February 2026; Accepted 8 April 2026
Available online 10 April 2026

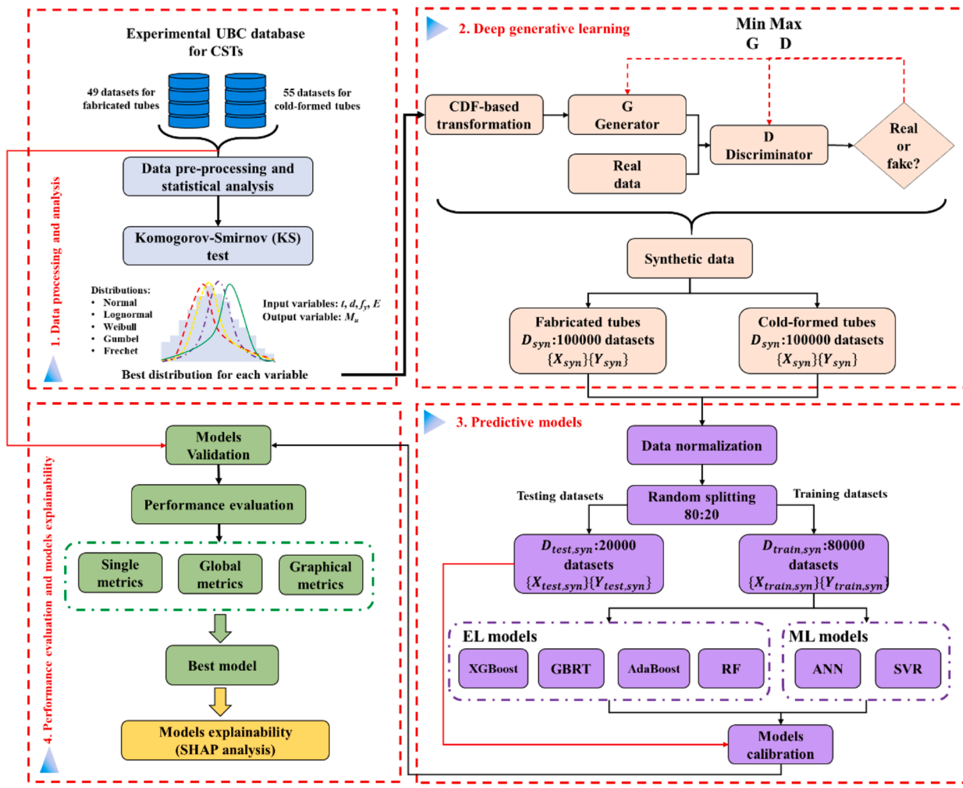

Fig. 1. Proposed framework using deep generative based ML & EL models to predict UCB for CSTs.

Table 1
Statistical description of the used database for fabricated circular steel tubes.

Statistical metrics	Input variables			Output	
	t (mm)	d (mm)	f_y (MPa)	E (MPa)	M_u (kN·m)
X_{max}	26,6	610	434	210	1892,7
X_{Q1}	3,9	168	304	200,25	48,3
X_{median}	6,4	406	342	210	306,1
X_{Q3}	12,9	458	378	210	918,3
X_{mean}	8,25	346,88	342,96	205,75	544,84
X_{SD}	6,27	169,05	50,21	4,92	576,14
X_{min}	0,76	89	245	198,94	1,6

Table 2
Statistical description of the used database for cold-formed circular steel tubes.

Statistical metrics	Input variables			Output	
	t (mm)	d (mm)	f_y (MPa)	E (MPa)	M_u (kN·m)
X_{max}	3,35	110,4	473	218	10,6
X_{Q1}	2,29	60,65	389	191,2	4
X_{median}	2,52	89,1	408	200	5,4
X_{Q3}	2,95	99,4	414	211	7,65
X_{mean}	2,43	81,37	408,87	200,74	5,83
X_{SD}	0,59	19,81	29,5	10,42	2,47
X_{min}	0,9	33,6	365	182	0,80

and contact nonlinearity (e.g. tube interaction with other parts causing deformation). Such factors contribute to a highly complex and nonlinear dynamic structural response, making predicting buckling behavior particularly challenging. Under pure bending, CSTs experience ovalization, where the initially circular cross-section gradually deforms into an oval shape [6]. The deformation is primarily caused by tensile and compressive stresses distributed across the cross-section, leading to a reduction in stiffness and inducing nonlinear structural behavior [7]. Consequently, predicting the ultimate bending capacity (UBC) of CSTs is highly complex due to the material's nonlinear response, the intricate cross-section behavior, and the often substantial applied loads. Accurate assessment of UBC is crucial, as any deformation can result in failures leading to severe environmental, economic, and safety risks. This underscores the necessity of developing accurate predictive framework to ensure the reliable performance and safe management of CSTs in structural applications.

Conducting experimental tests to determine the UBC for each type and grade of CSTs is often challenging due to the high costs, time constraints, and the need for specialized testing rigs. Alternatively, various predictive models have been developed, comprising national and international standards, as well as correlation proposed by researchers. Among the established design codes and standards widely used to estimate the UBC are the Australian New Zealand Standards (AS/NZS 4600) [8], Australian Standards (AS 4100) [9], American Institute of Steel Construction (AISC) [10], and Eurocode 3 [11]. These design codes provide empirical formulations based on experimental data and theoretical considerations, offering practical solutions for engineering applications. Although such models provide simple guidance for predicting UBC for CSTs, the predictive accuracy is limited due to the assumption of small degree of ovalization and deformed shape, which retains an ideal elliptical form. These assumptions simplify the UBC estimation, however, decrease the accurate representation of the material's response, especially at larger deformations. Researchers extended the predictive capabilities of such standards by developing correlations and mathematical models that incorporate additional deformation mechanisms [12]. Some models introduce plastic hinges at specific locations along the tube length, while others assume linear distribution of plasticity across the element [13]. These models may capture the material's deformation more accurately than the previous ones, although still subjected to idealized assumptions. Chen et al. [14] derived analytical equations for the UBC of steel pipes using Hencky's total strain theory and an elastic-linear strain hardening model. Their findings demonstrate that incorporating strain hardening indicates a better agreement with the test results compared to the design code of the pipelines and tubular

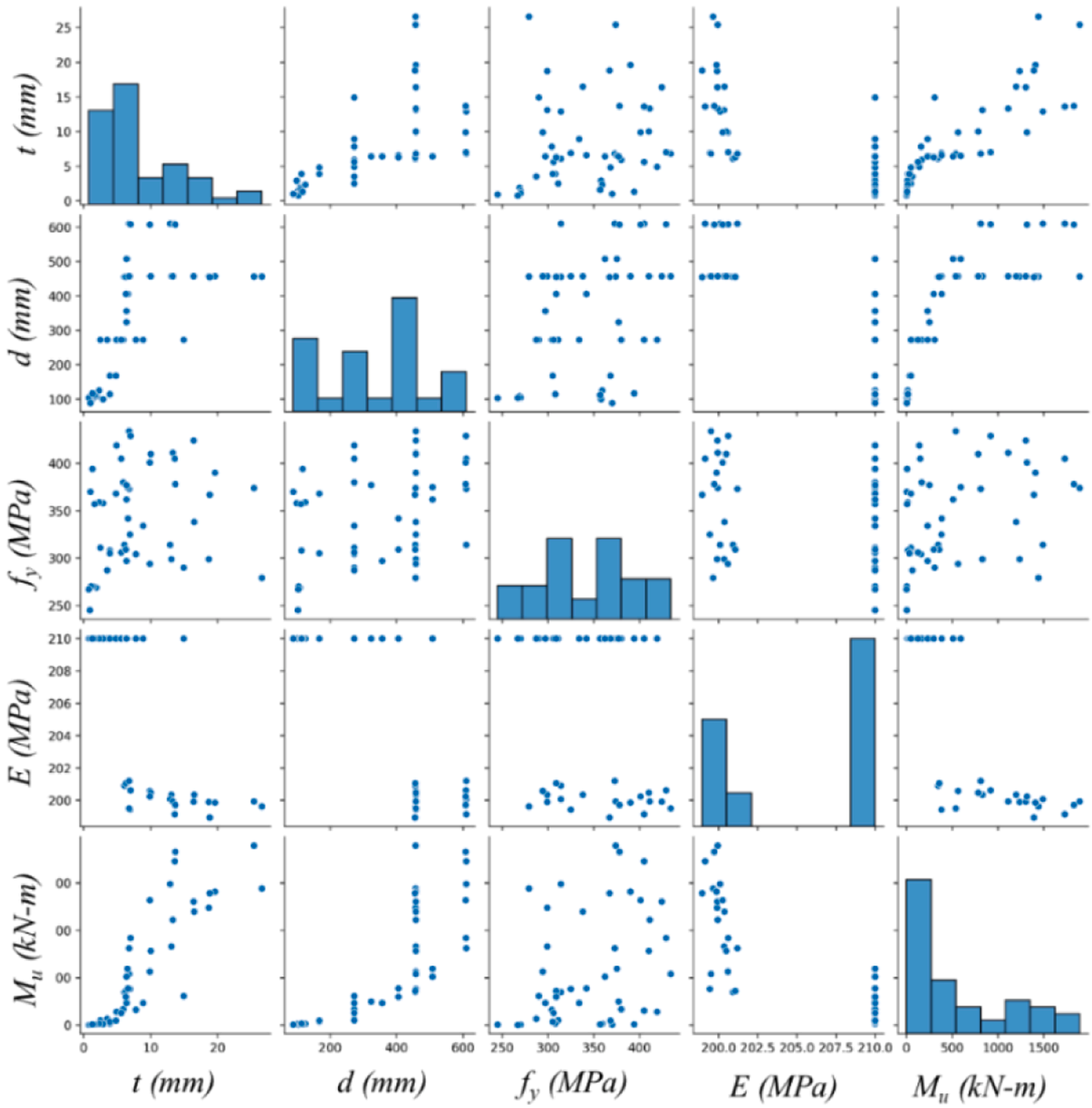

Fig. 2. Pairplot representation of the used database for fabricated circular steel tubes.

structures, where strain hardening is neglected. In another study, Knupp et al.[15]. developed an analytical solution for perforated tubular structures under combined bending and axial stresses. The study concluded that considering strain hardening increases the UBC compared to the elastic-perfectly plastic material assumption. Although such type of mathematical developments are valuable, their applicability is restricted due to the assumptions and simplifications involved. A more detailed understanding of structural response can be achieved through numerical simulations, particularly using finite element analysis (FEA) [16]. Han et al. [17] used FEA based ABAQUS software to study the torsional behavior of concrete-filled steel tubes (CFST), where the modelling showed high agreement with the test results. Another similar study was conducted by Wang et al. [18] where a FEA model was developed to investigate the performance of CFST members. The FEA results and test data were compared, verifying good match between the two. Zhang and Zhong [19] utilized FEA to efficiently predict the section flattening phenomenon of cross-sectional ovalization of tubes under rotary straightening. These studies illustrate the ability of FEA to provide a more thorough model for the material behavior and geometric effects, enabling the anticipation of both small and large deformations with higher accuracy. Even though FEA-based simulations can be beneficial, the main drawback is the high computational cost due to the required details and the high complicated modeling. Therefore, more flexible techniques are required to build a robust framework to deal with this engineering challenge.

Artificial intelligence (AI), particularly machine learning (ML) and ensemble learning (EL) techniques become indispensable tools for addressing challenging structural engineering problems by developing adaptive models capable of functioning without relying on depth predefined physics knowledge [20–24]. In contrast to traditional computing models, which reply on modified mathematical formulations developed based on experimental data and simple fitting techniques,

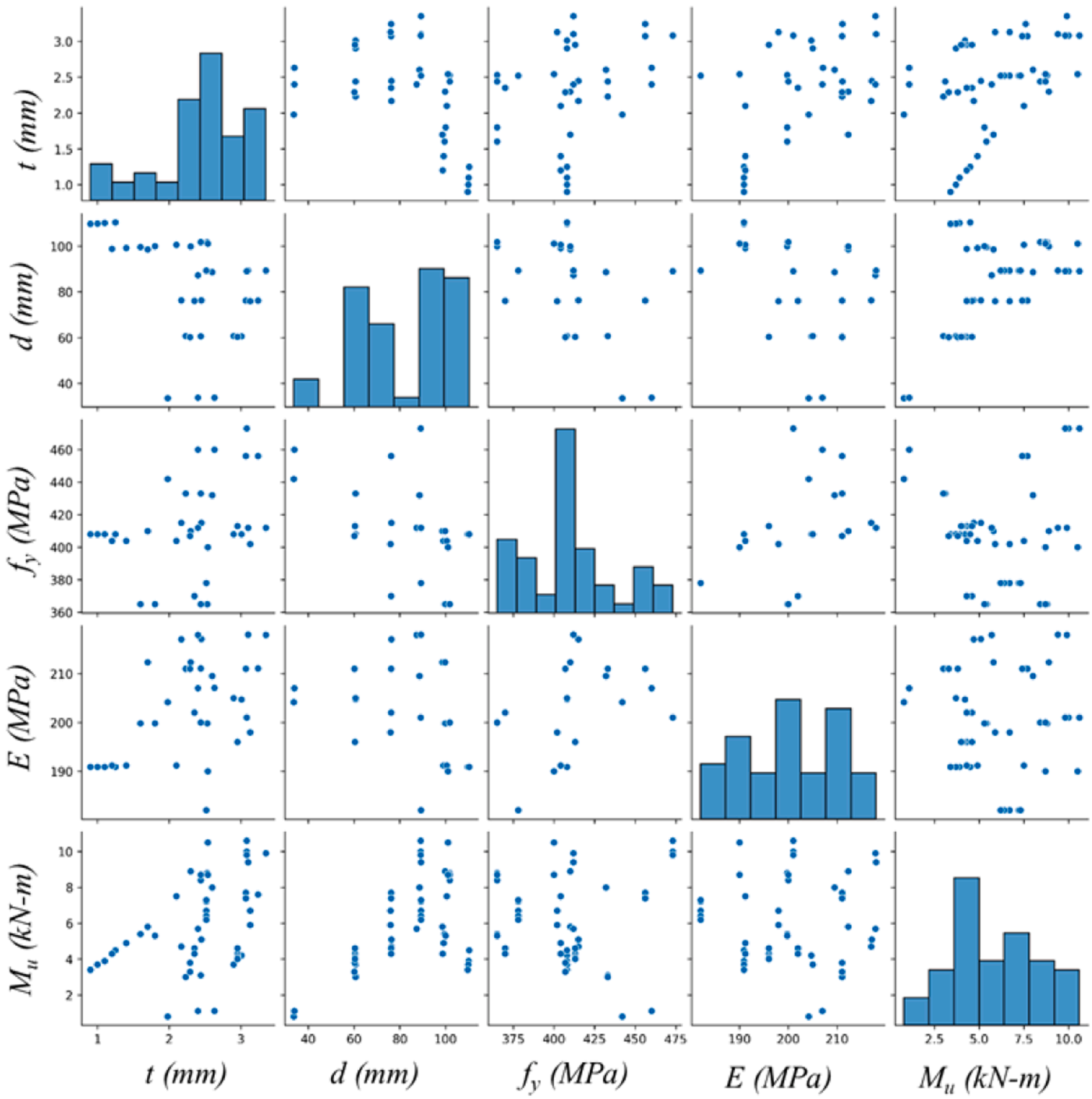

Fig. 3. Pairplot representation of the used database for cold-formed circular steel tubes.

ML/EL models can deal with different data to identify complex patterns and create predictive models that approximate more efficient solutions [25,26]. Numerous studies have explored ML potentials to predict UCB in different structural elements. Xu et al. [27] applied Random Forest (RF) and Extreme Gradient Boosting (XGBoost) to predict the UCB of cold-formed stainless steel tubular columns, using a dataset composed of 322 samples, including 165 samples with square hollow sections and 157 samples of other column types. Their study findings indicated that RF and XGBoost algorithms outperformed the Eurocode predictions. Basarir et al. [28] investigated the ultimate pure bending of concrete-filled steel tubes using Linear Multiple Regression (LMR), Nonlinear Multiple Regression (LNMR) and Adaptive Neuro-Fuzzy Inference Systems (ANFIS) using a database of 72 pure bending tests. The study's results demonstrated that ANFIS provided accurate predictions, surpassing both regression models and traditional design codes. Shahin and Elchalakani [29] explored the use of Artificial Neural Networks (ANNs) to predict the UBC of CSTs, utilizing 49 tests on fabricated tubes and 55 cold-formed tubes, where ANNs provided superior accuracy compared to various established design codes including Eurocode 3, AS/NZS 4600, AS 4100 and ASIC. In similar study done by Simwanda et al. [30], ten distinct ML/EL models were utilized to predict the material behaviour of slotted perforated cold-formed steel beams under distortional buckling (i.e. ANN, Support Vector Regression (SVR), k-nearest neighbors (k-NN), and Decision Tree (DT); RF, Adaptive Boosting (AdaBoost), Gradient Boosting Machine (GBM), Light Gradient Boosting machine (LightGBM), Categorical Boosting (CatBoost), and XGBoost). It was concluded that the developed models provided high predictive accuracy, outperforming traditional design codes, including AS/NZS 4600. Recently, Ben Seghier et al. [31] employed improved RF models by incorporating the Particle Swarm Optimization (PSO), Ant Colony Optimization (ACO) and Whale Optimization Algorithm (WOA) to predict the UCB of CSTs based on 104 pure bending tests. The hybrid

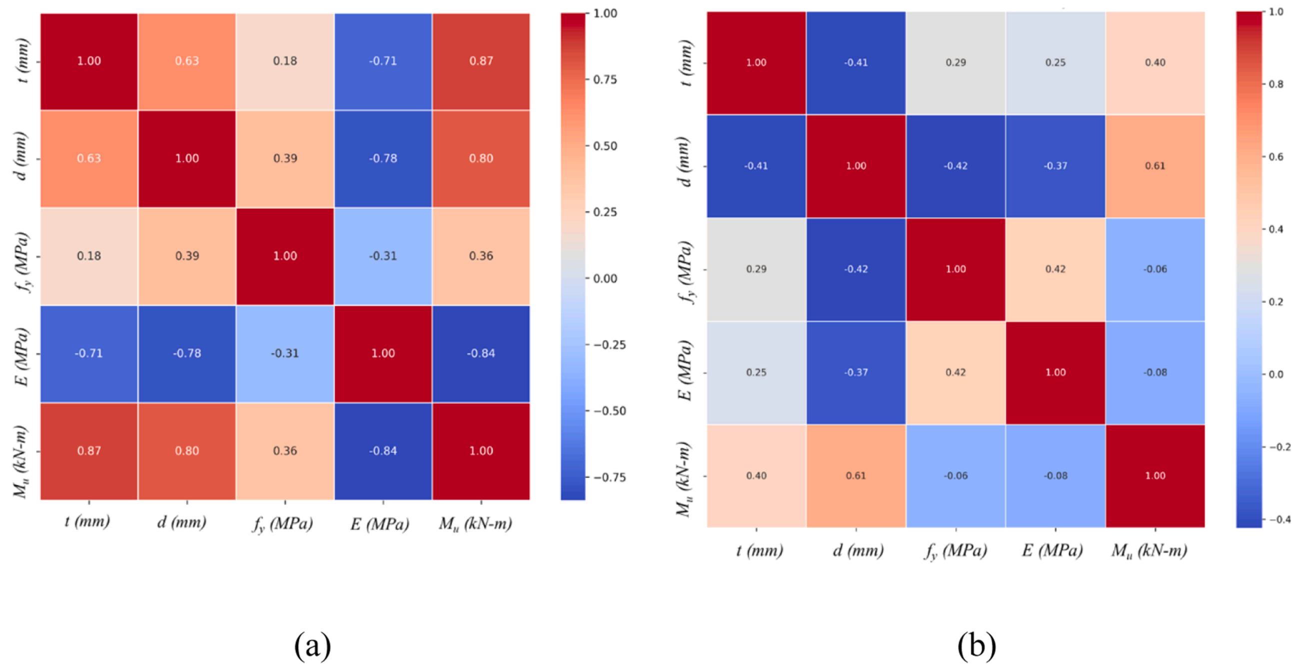

Fig. 4. Heatmap based Pearson correlation matrix between the used CST variables. (a) Fabricated tubes and (b) Cold-form tubes.

Table 3
KS-test results for fabricated circular tubes.

Distributions	KS-test				
	Input variables				Output
	t (mm)	d (mm)	f_y (MPa)	E (MPa)	M_u (kN·m)
Normal	0212	0208	0147	0377	0201
Lognormal	0113	0217	0141	**0369**	0171
Weibull	0132	0217	**0130**	0381	**0144**
Gumbel	0142	0218	0144	0373	0149
Frechet	**0096**	**0175**	0151	0571	0252

Note: numbers in bold represent the best results.

Table 4
KS-test results for cold-formed circular tubes.

Distributions	KS-test				
	Input variables				Output
	t (mm)	d (mm)	f_y (MPa)	E (MPa)	M_u (kN·m)
Normal	0172	0170	0200	0128	0113
Lognormal	0172	0170	0452	0497	0101
Weibull	0147	0150	0193	0128	0097
Gumbel	0229	0173	0189	0122	**0076**
Frechet	**0146**	**0138**	**0164**	**0121**	0108

Note: numbers in bold represent the best results.

RF-WOA model demonstrated the highest accuracy showcasing its potential as a valuable tool for structural analysis and design of CSTs. These studies demonstrate a promising future for the use of ML/EL in predicting nonlinear behavior in structural analysis, as well as structural engineering application in general. A common limitation among these studies is the relatively small size of the used databases, where this constrains the generalizability and robustness of the predictive models. However, due to the accompanying costs, undertaking a major experimental program to generate a significant experimental database is not feasible. Thus, combining current predictive models with AI-based frameworks to establish larger reliable databases can give a new paradigm for dealing with such structural engineering challenges.

This paper presents a new shifting paradigm based on deep generative, ML, and EL models to close the aforesaid gaps and accurately predict the UBC for CSTs. In the first stage, the Copula Generative Adversarial Networks Synthesizer is introduced for the first time to produce credible databases using limited data from two types of CSTs based on the manufacturing process, namely cold-formed and fabricated steel tubes. This necessitates a thorough examination of the limited datasets, including correlation and variability analysis, as well as determining the best fit distribution for each variable, which is accomplished using the Kolmogrov-Smirnov test. In the second stage, six predictive models, including ML and EL models, are used to develop UBC predictive models. The outcomes of the trained models is thoroughly examined using multiple performance metrics to determine their accuracy and predictive capability. Finally, model explainability is also conducted to interpret the best performing model among the proposed ones, and examine the influence of input variables on the predictive model outcomes.

2. Methodology

2.1. Copula generative adversarial networks synthesizer (CopulaGAN)

Generative Adversarial Networks (GANs), introduced by Goodfellow et al. [32], utilize an adverbial learning model inspired by zero-sum game theory to generate synthetic data. This consists of two competing neural networks: the generator (G) and the discriminator (D). The first is an unsupervised neural network that learns the statistical characteristics of a given dataset and generates synthetic samples to deceive the second. This latter distinguishes the real generated sample datasets from the fake ones. The process between the two-phases is modeled as a *minimax* game, where D tends to maximize the detection of real data correctly, while G tend to minimize the detection rate by increasing the generation of credible data. The GAN process can be expressed mathematically as follows [33,34]:

$$min_G max_D V(D,G) = E_{x\sim Pdata(\boldsymbol{x})}[logD(\boldsymbol{x})] + E_{z\sim P_z(\boldsymbol{z})}[\log(1 - D(G(\boldsymbol{z})))] \tag{1}$$

where $\boldsymbol{x}$ is the original dataset, while $\boldsymbol{z}$ denotes the decimator prediction

Table 5
The formulas and descriptions of the statistical evaluation metrics utilized in this study.

	Metric	Definition	Equation	Description
Single	RMSE	Root mean squared error	$\sqrt{\frac{1}{n}\sum_{i=1}^{n}\left(M_u^{exp,\ i}-M_u^{pre,\ i}\right)^2}$	Measures the average magnitude of prediction errors, where lower value indicates better model performance.
	MAPE	Mean absolute percentage error	$\frac{100\%}{n}\sum_{i=1}^{n}\left\|\frac{\left(M_u^{exp,\ i}-M_u^{pre,\ i}\right)}{M_u^{exp,\ i}}\right\|$	Represents the relative error in percentage terms, with lower value indicating higher accuracy.
	MAE	Mean absolute error	$\frac{1}{n}\sum_{i=1}^{n}\left\|\left(M_u^{exp,\ i}-M_u^{pre,\ i}\right)\right\|$	Quantifies the average absolute difference between prediction and actual values, where lower values suggest higher accuracy.
	NSE	Nash–Sutcliffe efficiency	$1-\frac{\sum_{i=1}^{n}\left(M_u^{exp,\ i}-M_u^{pre,\ i}\right)^2}{\sum_{i=1}^{n}\left(M_u^{exp,\ i}-M_{u,\ avg}^{exp}\right)^2}$	Evaluates the model performance using the mean of observed values, where more the value is close to unit more the accuracy is high.
	WI	Willmott index	$1-\frac{\sum_{i=1}^{n}\left(M_u^{exp,\ i}-M_{u,\ rate}^{pre,\ i}\right)^2}{\sum_{i=1}^{n}\left(\left\|M_u^{pre,\ i}-M_{u,\ avg}^{exp}\right\|+\left\|M_u^{exp,\ i}-M_{u,\ avg}^{exp}\right\|\right)^2}$	Assesses the degree of agreement between experimental and predicted values, where values close to unit indicate strong agreement.
	R^2	Coefficient of determination	$1-\frac{\sum_{i=1}^{n}\left(M_u^{exp,\ i}-M_u^{pre,\ i}\right)^2}{\sum_{i=1}^{n}\left(M_u^{exp,\ i}-M_{u,\ avg}^{exp}\right)^2}$	Represents the proportion of variance, with values close to unit indicate high predictive ability of the model.
	DR	Discrepancy ratio	$Log\ \frac{M_u^{exp,\ i}}{M_u^{pre,\ i}}$	Measures the average logarithmic difference between predicted and observed values, where values closer to zero indicate better agreement.
Global	CI	Confidence index	$WI * NSE$	Measures the model's ability to correctly rank predictions related to actual values, with higher values indicating stronger agreement.
	U_{95}	Bias-variance	$1.96\sqrt{SD^2+RMSE^2}$	Quantifies prediction uncertainty, with lower values indicating more reliable results.
	OBJ	Objective function	$\left(\frac{n_{train}-n_{test}}{n_{train}+n_{test}}\right)\left(\frac{RMSE_{train}+MAE_{train}}{R^2_{train}}\right)+\left(\frac{2n_{test}}{n_{train}+n_{test}}\right)\left(\frac{RMSE_{train}+MAE_{train}}{R^2_{test}}\right)$	Gives indication for the model performance, with lower values representing high global accuracy.
	PI	Performance index	$\left(\frac{1}{j}\right)\left(\frac{RMSE_{model}}{RMSE_{max}}+\frac{MAE_{model}}{MAE_{max}}+\frac{OBJ_{model}}{OBJ_{max}}+\frac{U_{95,\ model}}{U_{95,\ train}}+\frac{R^2_{min}}{R^2_{model}}+\frac{NSE_{min}}{NSE_{model}}+\frac{WI_{min}}{WI_{model}}+\frac{CI_{min}}{CI_{model}}+\ldots\right)$	Gives an indication for the overall performance of the model.

Note: $M_u^{exp,\ i}$ denotes the *i th* synthetic/experimental value of the UBC for CST, while $M_u^{pre,\ i}$ is the *i th* predicted value of UBC for CST. $M_{u,\ avg}^{pre}$ represent the average value of the predicted UBC, while $M_{u,\ avg}^{exp}$ represents the average value of the synthetic/experimental UBC. n is the sample number, while j is the total number of metrics.

Table 6
Comparative statistics between the original and synthetic datasets for the fabricated circular steel tubes.

	Inputs								Output	
	t (mm)		*d (mm)*		f_y *(MPa)*		*E (MPa)*		M_u *(kN·m)*	
	Org. data	Synth. data	Org. data	Synth. data	Org. data	Synth. data	Org. data	Synth. data	Org. data	Synth. data
Max	26,6	26,6	610	610	434	434	210	210	1892,7	1892,7
(R_e %)	*(0,00 %)*		*(0,00 %)*		*(0,00 %)*		*(0,00 %)*		*(0,00 %)*	
Q1	3,9	4,41	168	206	304	301	200,3	200,3	48,3	64,2
(R_e %)	*(−13,08 %)*		*(−22,62 %)*		*(0,99 %)*		*(0,00 %)*		*(−32,92 %)*	
Median	6,4	6,26	406	411	342	334	210	209,93	306,1	302,4
(R_e %)	*(2,19 %)*		*(−1,23 %)*		*(2,34 %)*		*(0,04 %)*		*(1,21 %)*	
Q3	12,9	12,64	458	463	378	378	210	210	918,3	1064,5
(R_e %)	*(2,02 %)*		*(−1,09 %)*		*(0,00 %)*		*(0,00 %)*		*(−15,92 %)*	
Mean	8251	8377	346,88	352,86	342,96	339,97	205,8	205,82	544,84	541,51
(R_e %)	*(−1,52 %)*		*(−1,72 %)*		*(0,87 %)*		*(−0,01 %)*		*(0,61 %)*	
SD	6335	5783	170,81	157,73	50,733	46,01	4972	4855	582,11	559,14
(R_e %)	*(−21,40 %)*		*(0,74 %)*		*(6,59 %)*		*(7,18 %)*		*(2,86 %)*	
Min	0,76	0,76	89	89	245	245	198,9	198,9	1,6	1,6
(R_e %)	*(0,00 %)*		*(0,00 %)*		*(0,00 %)*		*(0,00 %)*		*(0,00 %)*	

of the generated sample. $V(D,G)$ represents the *minimax* game value function, while $P_z(\boldsymbol{z})$ is predefined noise variables.

The Conditional Tabular (CTGAN) model is a specialized GAN variant designed for tabular data, where handling non-Gaussian and multimodal distributions is possible [35]. CTGAN ensures preserving the structural characteristics of the original dataset in the generated

Table 7
Comparative statistics between the original and synthetic datasets for the cold-formed circular steel tubes.

	Inputs								Output	
	t (mm)		*d (mm)*		f_y *(MPa)*		*E (MPa)*		M_u *(kN·m)*	
	Org. data	Synth. data	Org. data	Synth. data	Org. data	Synth. data	Org. data	Synth. data	Org. data	Synth. data
Max	3,35	3,35	110,4	110,4	473	473	218	218	10,6	10,6
(R_e %)	*(0,00 %)*		*(0,00 %)*		*(0,00 %)*		*(0,00 %)*		*(0,00 %)*	
Q1	2,29	2,32	60,65	65,78	389	386	191,2	194,7	4	4,2
(R_e %)	*(−1,31 %)*		*(−8,46 %)*		*(0,77 %)*		*(−1,83 %)*		*(−5,00 %)*	
Median	2,52	2,5	89,1	86,465	408	407	200	200,9	5,4	5,2
(R_e %)	*(0,79 %)*		*(2,96 %)*		*(0,25 %)*		*(−0,45 %)*		*(3,70 %)*	
Q3	2,95	2,91	99,4	98,03	414	413	211	208,1	7,65	7,8
(R_e %)	*(1,36 %)*		*(1,38 %)*		*(0,24 %)*		*(1,37 %)*		*(−1,96 %)*	
Mean	2428	2467	81,37	81,684	408,87	406,815	200,74	201,013	5831	5833
(R_e %)	*(−1,60 %)*		*(−0,39 %)*		*(0,50 %)*		*(−0,14 %)*		*(−0,03 %)*	
SD	0599	0536	19,99	18,008	29,767	27,311	10,517	8433	2488	2128
(R_e %)	*(10,47 %)*		*(9,91 %)*		*(8,25 %)*		*(19,82 %)*		*(14,48 %)*	
Min	0,9	0,9	33,6	33,6	365	365	182	182	0,8	0,8
(R_e %)	*(0,00 %)*		*(0,00 %)*		*(0,00 %)*		*(0,00 %)*		*(0,00 %)*	

synthetic data by introducing model-specific normalization for continuous variables and one-hot encoding for categorical variables. Furthermore, conditional generation and training-by-sampling help reducing the mode collapse and ensures balanced category representation. CopulaGAN [36] enhances CTGAN by using Gaussian copula transformations, which improves the learning process effectiveness and efficiency. The Copula transformations simplify the model's task of capturing complex correlations between the variables by utilizing the cumulative distribution function (CDF) and transforming the dataset into a uniform distribution before feeding it into GAN. Thus, CopulaGAN is able to generate realistic synthetic data without requiring detailed knowledge of the original dataset.

2.2. Predictive AI based modeling techniques

In this study, two machine learning (ML) and four ensemble learning (EL) techniques are utilized to predict the UBC for CSTs, which are briefly described in the following subsections.

2.2.1. Machine learning (ML) techniques

2.2.1.1. Artificial neural network (ANN). ANN is well-known ML technique used to handle high-dimensional nonlinear problems [37,38]. By utilizing artificial neurons to replicate the biological nervous system in processing information, ANN structures mimic the human brain, and composed of three interconnected layers, i.e. the input, hidden, and output layers, each provide specific number of neurons. After receiving the input data vector, $\boldsymbol{X}$, the input layer sends the raw data to the hidden layer. This latter performs the calculations and transmit the results to the output layer, which determines the final predicted values, $\boldsymbol{Y}$. This can be expressed mathematically as [39]:

$$\boldsymbol{Y} = \sum_{j=1}^{n} w_j h_j + \boldsymbol{b} \tag{2}$$

where w_j denotes the weight between *j-th* hidden neuron and the output neuron, while $\boldsymbol{b}$ is the output layer bias. h_j represent the output of the *j-th* hidden layer, which can be expressed as:

$$h_j = f\left(\sum_{i=1}^{n} w_{ji} X_i + b_j\right)\ ,\ i = 1, 2, 3, \ldots., n \tag{3}$$

where, w_{ji} represents the weight between the $i-th$ input neuron and the $j-th$ hidden neuron, x_i denotes the $i-th$ input neuron, while b_j is the bias of the $j-th$ hidden neuron. The activation function, represented by f (such as hyperbolic, tangent, or sigmoid curves), can be selected by trial and error according on to which one best fits the problem.

2.2.1.2. Support vector regression (SVR). SVR is a supervised ML technique commonly used to solve nonlinear regression problems [40,41]. SVR uses linear regression to determine an optimal hyperplane that fits the best the data within a predefined margin ε, after identifying important data points, called vector [42]. Consequently, the SVR model with the maximum number of data points inside this margin is considered generalized. However, it is challenging to identify an appropriate hyperplane in the original feature space as real-world data are frequently nonlinear and randomly distributed. To get around this, SVR uses a kernel function (such as the Gaussian function or radial basis function) to move the original problem to a higher feature space [43]. This allows for the computation of an optimal linear regression function in the new feature space. The approximating function using SVR is indicated in Eq. (4) [44].

$$\boldsymbol{Y} = \omega.\varphi(\boldsymbol{X}) + \boldsymbol{b} \tag{4}$$

where $\boldsymbol{\omega}$ and $\boldsymbol{b}$ are the weight and the bias vectors, respectively. $\varphi()$ represents the kernel function, while $\boldsymbol{X}$ the input variable vector.

2.2.2. Ensemble learning (EL) techniques

2.2.2.1. Random forest (RF). RF is a well-known EL technique that combines multiple decision trees (DTs) to improve predictive accuracy and reduce overfitting [45]. In RF, each DT is trained independently using random subsets of the training data and randomly selecting a subset of features, so-called bootstrap sampling and feature randomness. The training is constructed in such a way that each successive DT tries to minimize the error from the preceding DT, meaning that each tree is built upon the outcome of other ones. This process will continue

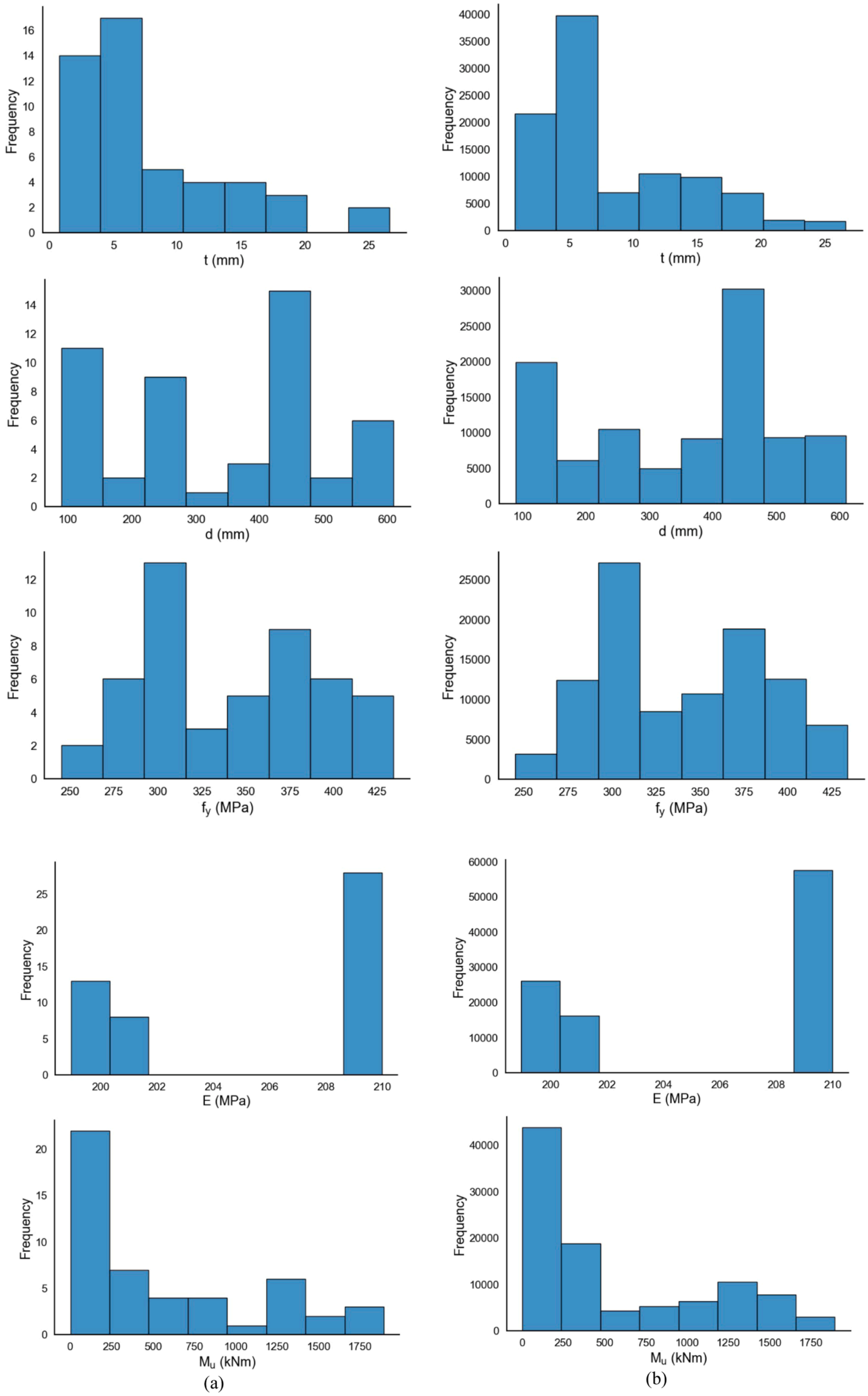

Fig. 5. Data distribution for each variable from the (a) original and (b) synthetic datasets of the fabricated circular steel tubes.

iteratively, increasing the number of trees in the forest, and thus increasing the RF accuracy. The final prediction output is calculated based on averaging the outputs of each DT in regression tasks [46]. As a result, the variance is reduced, the prediction generalization is improved, while overfitting risks are mitigated. The RF process can be expressed mathematically as follows [47]:

$$\boldsymbol{Y} = \frac{1}{N}\sum_{i=1}^{N} Y_i(\boldsymbol{X}') \tag{5}$$

where $\boldsymbol{Y}$ represents the target output, N is the total number of trees. Y_i denotes the i th individual decision tree, while $\boldsymbol{X}'$ represents the unknown instances.

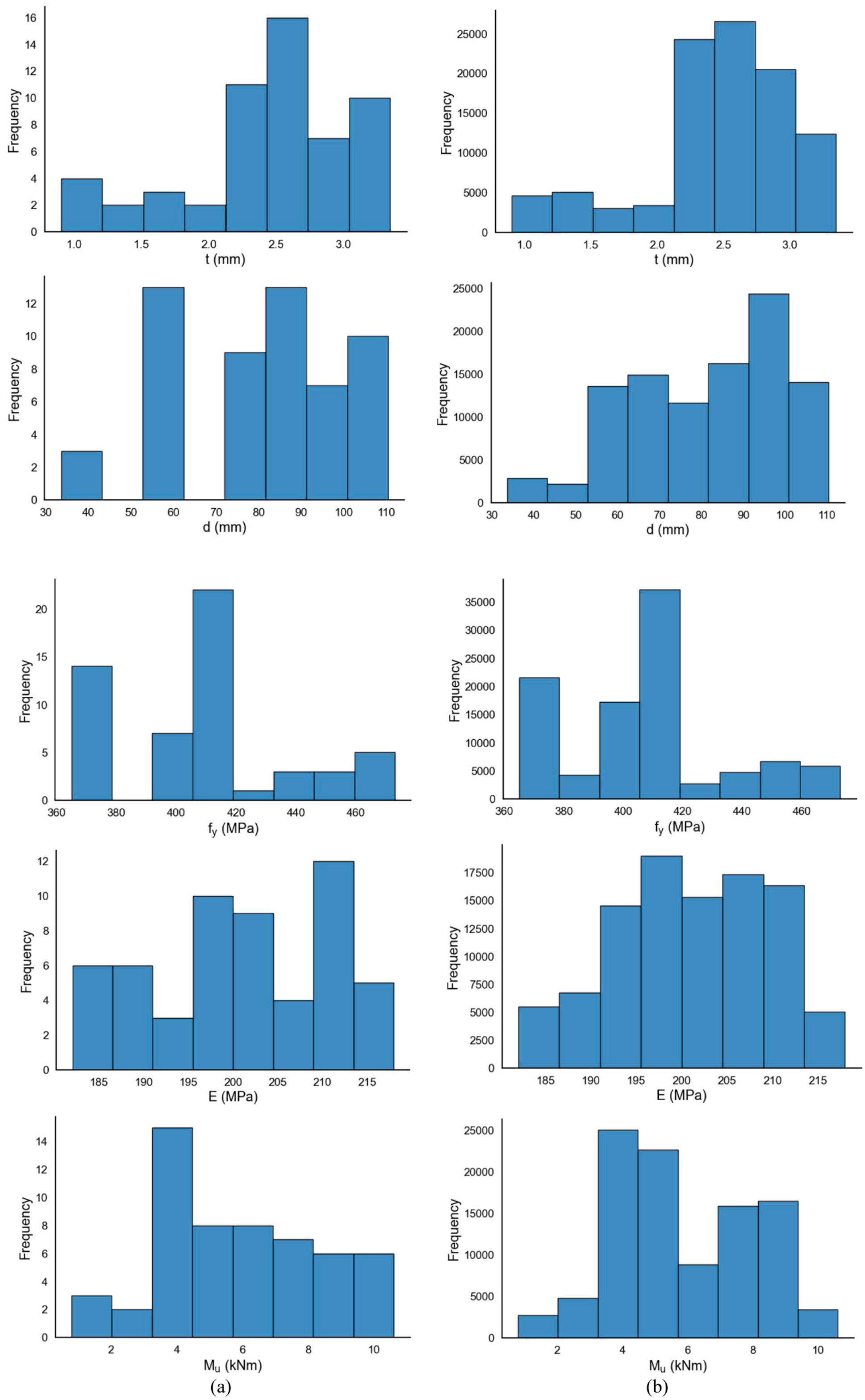

Fig. 6. Data distribution for each variable from the (a) original and (b) synthetic datasets of the cold-formed circular tubes.

2.2.2.2. Adaptive boosting (AdaBoost). Unlike bagging (e.g. RF), AdaBoost utilizes the concept of boosting to improve the overall model performance, by merging multiple weak learners (e.g., DT) that trained on a sequential order using different subsets of the data. This process can be expressed as [48]:

$$F_T(\boldsymbol{X}) = \sum_{t=1}^{T} f_t(\boldsymbol{X}) \tag{6}$$

where F_T represents the weak learner, whereas $\boldsymbol{X}$ is the input variables' vector. Initially, AdaBoost assigns equal weights to all training datasets, with each weight signifying the importance of the corresponding

Table 8
Results of the performance evaluation for the fabricated circular steel tubes using the ML & EL models.

Phase	Single metrics	ML models				EL models	
		SVR	ANN	RF	AdaBoost	GBRT	XGBoost
Training	**RMSE**	224,6102	193,9925	176,6120	153,5216	146,4800	**131,8125**
	MAPE	**202,1951**	389,9290	412,3842	358,8832	358,2399	357,8802
	MAE	125,3731	114,1412	102,9867	87,3877	85,0341	**80,2396**
	NSE	0,8386	0,8796	0,9002	0,9246	0,9314	**0,9444**
	WI	0,9558	0,9674	0,9730	0,9799	0,9816	**0,9853**
Testing	**RMSE**	223,5599	193,7840	188,5229	184,2151	166,0071	**157,7568**
	MAPE	**186,3033**	363,6038	388,1006	352,5220	349,9712	349,8127
	MAE	124,8580	114,3730	107,9728	101,2708	94,0127	**91,4491**
	NSE	0,8401	0,8799	0,8863	0,8914	0,9118	**0,9204**
	WI	0,9563	0,9675	0,9692	0,9708	0,9762	**0,9787**
Validation	**RMSE**	379,4417	198,8312	195,1945	200,8392	132,7676	**77,9627**
	MAPE	**64,8882**	248,8395	212,0192	932,9969	381,2663	449,2575
	MAE	238,7067	134,8048	118,2885	178,2569	78,7456	**54,7375**
	NSE	0,9094	0,8809	0,8852	0,8785	0,9469	**0,9817**
	WI	0,8231	0,9733	0,9633	0,9594	0,9844	**0,9951**

*Numbers in bold represent the best result based on the statistical metrics.

Table 9
Results of the performance evaluation for the cold-formed circular steel tubes using the ML & EL models.

Phase	Single metrics	ML models					EL models
		SVR	ANN	RF	AdaBoost	GBRT	XGBoost
Training	**RMSE**	1,0946	0,9901	0,9608	0,8591	0,7975	**0,6890**
	MAPE	12,7671	12,8384	12,2949	10,6299	11,4429	**10,9956**
	MAE	0,6721	0,6678	0,6414	0,5617	0,5887	**0,5522**
	NSE	0,7351	0,7833	0,7959	0,8368	0,8594	**0,8950**
	WI	0,9265	0,9368	0,9401	0,9532	0,9645	**0,9767**
Testing	**RMSE**	1,0983	1,0026	1,0023	0,9737	0,9473	**0,8646**
	MAPE	12,6993	12,8611	12,6057	**11,8732**	13,1180	13,0159
	MAE	0,6722	0,6731	0,6625	**0,6309**	0,6985	0,6964
	NSE	0,7345	0,7788	0,7789	0,7914	0,8025	**0,8355**
	WI	0,9266	0,9357	0,9350	0,9397	0,9499	**0,9650**
Validation	**RMSE**	0,8818	0,9260	0,8591	0,7173	0,6713	**0,5402**
	MAPE	13,2410	16,4378	16,5679	12,8125	12,0967	**9,2071**
	MAE	0,6482	0,7204	0,6496	0,5815	0,5083	**0,4269**
	NSE	0,8721	0,8590	0,8786	0,9154	0,9259	**0,9520**
	WI	0,9592	0,9521	0,9599	0,9759	0,9769	**0,9861**

*Numbers in bold represent the best result based on the statistical metrics.

dataset. During the sequential iterative training process, where AdaBoost evaluates the prediction performance and assigns it a weight; the higher the error, the higher the weight. The dataset weights are then updated, making mispredicted datasets more significant, where to lower the overall training error, a new weak learner is created. This is expressed as follows [49]:

$$E_t = \sum_i E[F_{t-1}(X_i) + \alpha_t h(X_i)] \tag{7}$$

where E_t is the weak learner derived from previous iteration (i.e. the total training error), whereas $\alpha_t h(X_i)$ is the improved weak learner. Through this iterative refinement, AdaBoost progressively reduces errors and enhances the overall model performance.

2.2.2.3. Gradient boosting regression tree (GBRT). GBRT is a similar sequential EL-technique for training a boosted weak learner well adapted to solve regression problems [50]. In contrast to the AdaBoost technique, GBRT improves the prediction results by fitting each weak learner to the negative gradient of the loss function (L) of the previous iteration [51]. Adding the obtained L to the weak learner will decrease the negative gradient direction (g_m) and enhance the model's predictive ability. This can be formulated as follows [52]:

$$F_m(\mathbf{X}) = F_{m-1}(\boldsymbol{X}) + argmin \sum_{i=1}^{n} L[y_i,\ F_{m-1}(X_i) + h(X_i)] \tag{8}$$

$$g_m = -\frac{\partial L[y, F_{m-1}(\boldsymbol{X})]}{\partial F_{m-1}(\boldsymbol{X})} \tag{9}$$

where $\boldsymbol{X}$ represents the input variables' vector , while *h(**X**)* denotes the base learner function. The minimum error will be reached when the *m-th* weak learner fits g_m of the cumulative L.

2.2.2.4. Extreme gradient boosting (XGBoost). XGBoost is a robust version of sequential EL-techniques (i.e. updated version of AdaBoost and GBRT) that typically uses DT as a weak learner [53]. XGBoost is highly regarded as an efficient and flexible supervised model for solving complex regression engineering problems [54,55]. This EL-technique incorporates an objective function with an additional regularization term in the loss function (L) in order to smooth the final acquired weights and prevent over-fitting. Additionally, the loss function is optimized using gradient statistics of the first and second orders. Row and column sampling are also supported by XGBoost, which solve the over-fitting problem. Therefore, faster model exploration is possible due to the distributed and parallel computing. The objective function (*OF*) in XGBoost can be expressed as follows [53]:

$$OF = \sum_{i=1}^{n} L(\hat{y}_i,\ y_i) + \sum_{t=1}^{k} \omega(f_t) \tag{10}$$

where, ω denotes the regulation term, $\hat{y}_i$ is the *i-th* predicted outcome,

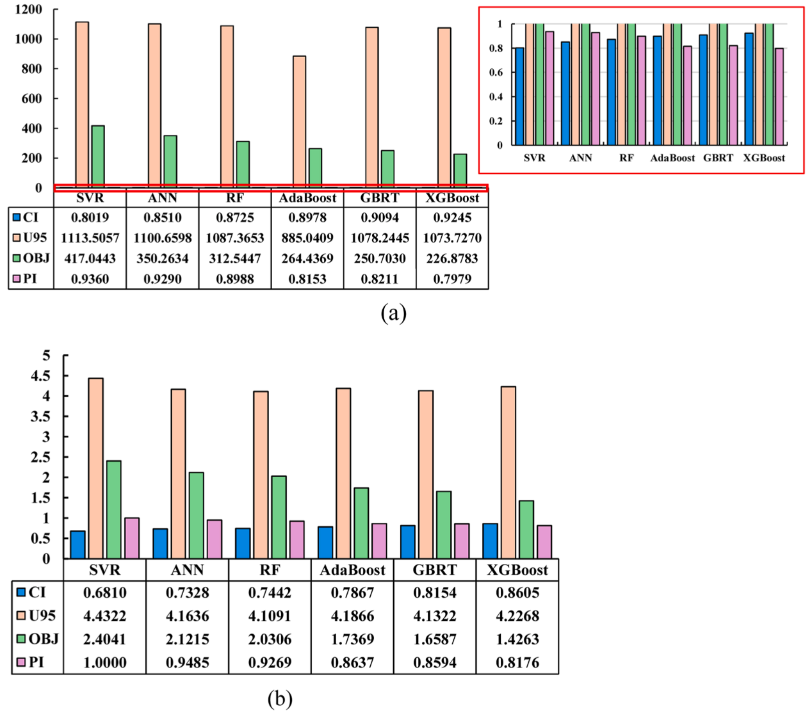

Fig. 7. Comparative results of the global performance metrics. (a) Fabricated circular steel tubes, (b) Cold –formed circular steel tubes.

while y_i stand for the *i-th* real experimental value. k and is n represent the total number of regression trees datasets, respectively.

3. Proposed framework

This study proposes a novel two-stage framework for developing a generalized path to accurate estimation of the UBC for CSTs based on limited experimental tests. The two-stage framework is achieved by four process-steps, as shown in Fig. 1. These steps include:

1. *Data pre-processing and analysis*: A statistical analysis is conducted on 104 collected experimental tests on UBC for CSTs [56–62]. The experimental test data are divided based on the manufacturing process into two groups: 55 for cold-formed tubes (manufactured by rolling a steel strip into a tube, then welding the seam) and 49 for fabricated tubes (manufactured by cutting, shaping, and welding steel plates into a tube). Section 3.1 provides a full statistical analysis of the databases. The Kolmogorov-Smirnov test is then used to determine the best-fitting distribution for each variable (Section 3.2), which will be employed in the following step.
2. *Deep generative learning*: Using the selected best distributions for the input and output variables, the CopulaGAN approach (Section 2.1) is utilized to generate 100,000 datasets for each type of CSTs that replicate the original data to develop robust predictive models.
3. *Predictive ML & EL model development*: The synthetic data is then normalized (Section 3.1) and then randomly divided into 80 % for training the ML models (ANN and SVR) and EL models (RF, AdaBoost, GBRT and XGBoost), Section 2.2, and 20 % for testing their performance. To mitigate overfitting and ensure robust modeling process, k-fold cross validation is applied throughout the training phase, where $k = 10$.
4. *Performance evaluation and model explainability*: The findings of the training, testing, and validation phases are used to undertake a comparative evaluation of the model's performance. The validation phase includes the model's performance based on the original data. Section 3.3 reports on the metrics used for this purpose, which included single, global, and graphical metrics. Finally, SHAP analysis is performed on the top-performing model to explain the relationship between input-output results and their dependencies.

3.1. Data description and preprocessing

Table 1 and Table 2 present the descriptive statistics, including the minimum ($\boldsymbol{X}_{\min}$), maximum ($\boldsymbol{X}_{\max}$), quartiles (i.e. $\boldsymbol{X}_{Qi}$, where Q1: 25 % quartile; Q2: 50 % quartile and Q3: 75 % quartile), mean ($\boldsymbol{X}_{\text{mean}}$) and standard deviation ($\boldsymbol{X}_{\text{SD}}$) of the used datasets. Table 1 displays the summary of the 49 datasets for fabricated circular steel tubes, whereas Table 2 reports the summary of the 55 datasets for cold-formed circular steel tubes. The tables consist of 4 input variables; thickness (t), diameter (d), yield strength (f_y), and Young's modulus (E), and one output-target-variable; ultimate bending moment (M_u). As evidenced by the statistical summary of both databases, the input and output variables have different ranges and scales. For example, amongst the variables, the SD ranges from 4.92 MPa (i.e. E) to 576.14 kN.m (i.e. M_u) for fabricated steel tubes and 0.59 mm (i.e. t) to 29.5 MPa (i.e. f_y) for cold-formed steel tubes. On the other hand, each variable's range is large; for example, M_u for fabricated steel tubes is [1,6 kN.m −1892,7 kN.m], whereas [0,80 kN.m −10,6 kN.m] for cold-formed steel tubes, indicating dispersion of the data. The quartiles are used to identify potential outliers based on the interquartile range ($IQR = Q3\text{-}Q1$), with observed data falling between the lower ($Q1\text{–}1.5IQR$) and upper ($Q3 + 1.5IQR$) bounds for all data. Furthermore, both databases are extremely small, therefore all information is required for the proposed deep generative framework.

As illustrated from the statistical reports, the datasets of the variables have significant different ranges and scales, which can pose challenges in developing an effective predictive model. This disproportionately misrepresent the problem complexity, and potentially led to imbalances that compromise the algorithm's performance. To mitigate this issue, normalization is applied to the datasets. This process ensures that all variables contribute equally to the predictive model development by scaling the data in the same range [0,1]. Data can be normalized using the following formula:

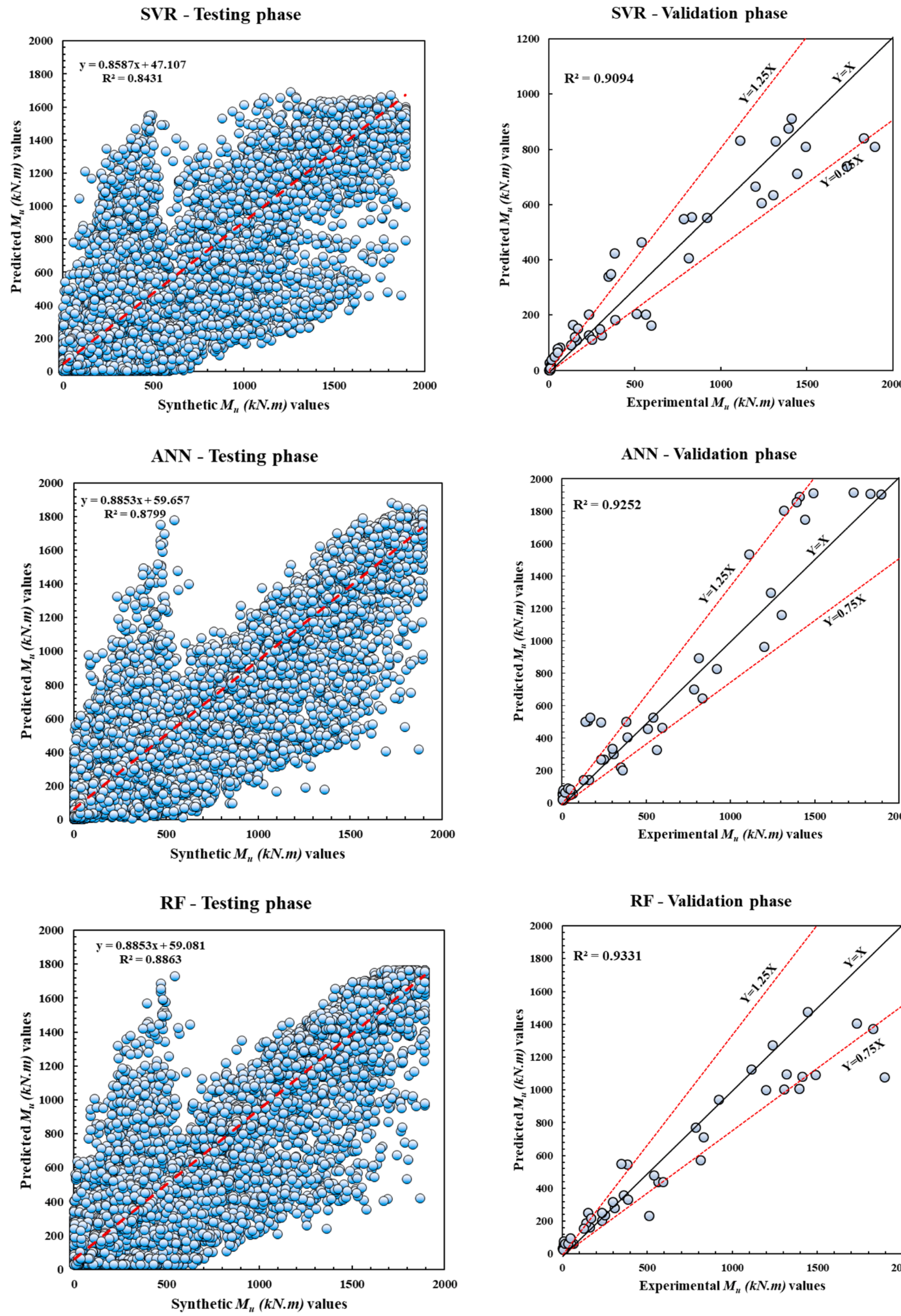

Fig. 8. Scatter plots of the proposed ML & EL models during the testing and validation phases for the fabricated steel tubes.

$$x' = \frac{x - x_{min}}{x_{max} - x_{min}} \tag{11}$$

where x represents the original value, x_{min} is the minimum value in the dataset, x_{max} is the maximum value in the dataset, and x' is the normalized value.

Fig. 2 and Fig. 3 present the pairplots illustrating the relationships between all the variables (i.e. t, d, f_y, E and M_u). Fig. 2 illustrates the pairplots of fabricated steel tubes, while Fig. 3 illustrates the pairplots of cold-formed steel tubes. Both pairplots exhibits distinct distributions and variable relationships, demonstrating the disparity and complexity of the datasets. This means that typical regression techniques will be unable to capture the problem's complexity due to a lack of data to investigate the relationship between the input-output variables. Thus, advanced models should be implemented.

Fig. 4 plots the Person correlation matrix in form of heatmap for all the used variables in the database, where Fig. 4(a) represents the heatmap of the fabricated circular steel tubes, while Fig. 4(b) represents the heatmap of the cold-formed circular steel tubes As observed, certain variables exhibit strong correlations, whereas other show moderate or weak relationships with the target variable (M_u). According to the results in Fig. 4(a), the tube thickness (t) has the highest correlation with the output variable (M_u), with a Pearson coefficient of 0.87, indicating positive proportionality, followed by the tube diameter (d) and Young's

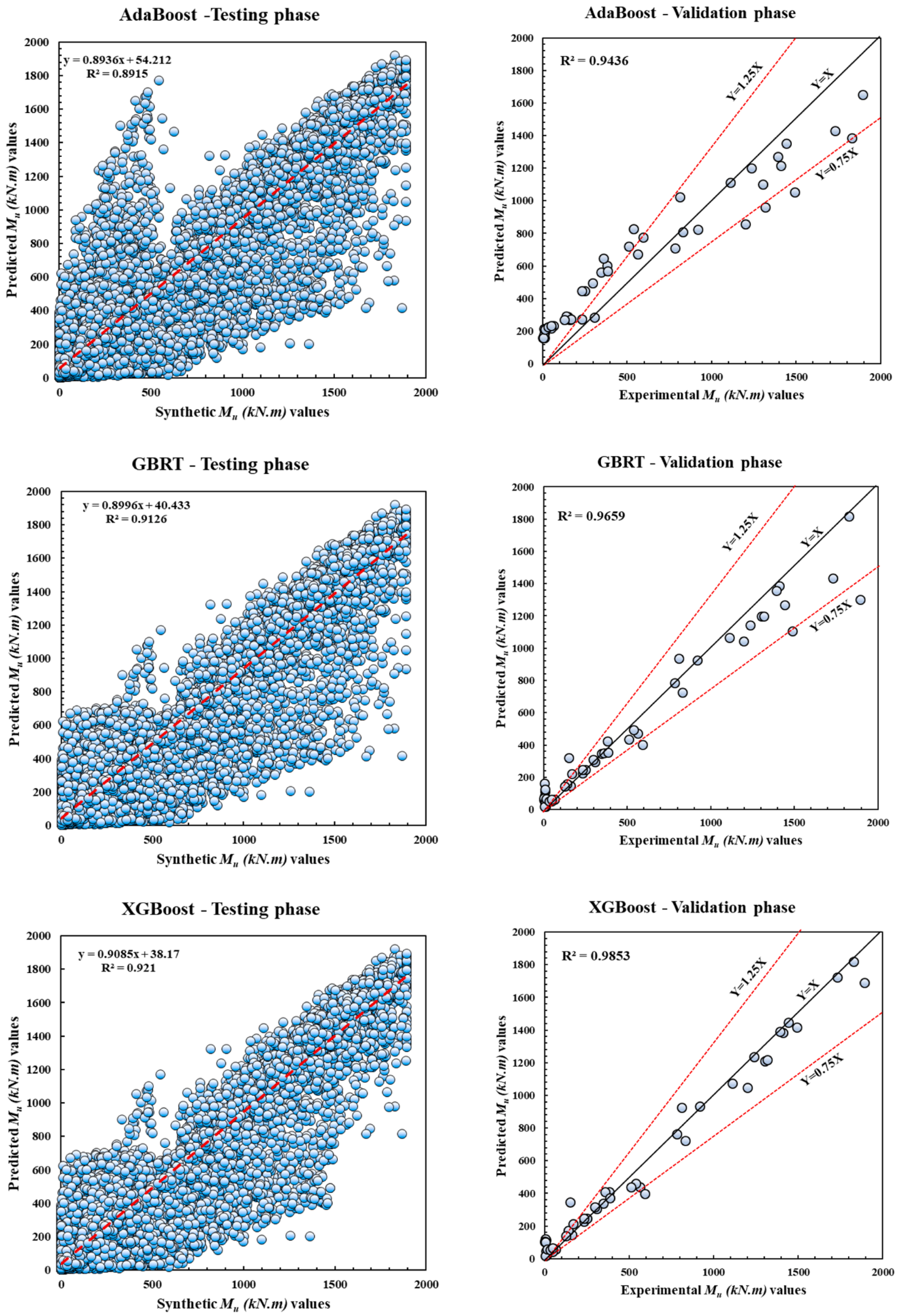

Fig. 8. (*continued*).

modulus (E), with values of 0.8 and −0.84, respectively, while the yield strength (f_y) showed moderate correlation with a value of 0.36. Conversely in Fig. 4(b), d exhibits the strongest correlation with M_u (0.61), whereas t indicates a moderate correlation (0.4). The remaining variables (E and f_y) show a very low correlation with the intended output, M_u. These variations highlight the differing influence of the input parameters on M_u for the two manufacturing process of circular steel tubes emphasizing the importance of separating the two databases.

3.2. Distribution analysis

In this study, the Komogorov-Smirnov (KS) test is employed to determine the best-fitting distribution for each variable in both databases. The KS-test is a statistical test used to assess the goodness-of-fit between an empirical dataset and a theoretical distribution [63,64]. It quantifies the maximum absolute difference between the empirical CDF of the dataset and the CDF of a given theoretical distribution. KS statistic *(D)* can be expressed as follows:

$$D_n = sup_{\boldsymbol{X}} |F_n(\boldsymbol{X}) - F(\boldsymbol{X})| \tag{12}$$

where $F_n(\boldsymbol{X})$ is the empirical CDF of the sample, $F(\boldsymbol{X})$ is the theoretical CDF of a vector of values ($\boldsymbol{X}$), whereas $sup_{\boldsymbol{X}}$ denotes the maximum of the absolute differences, and n is the sample size.

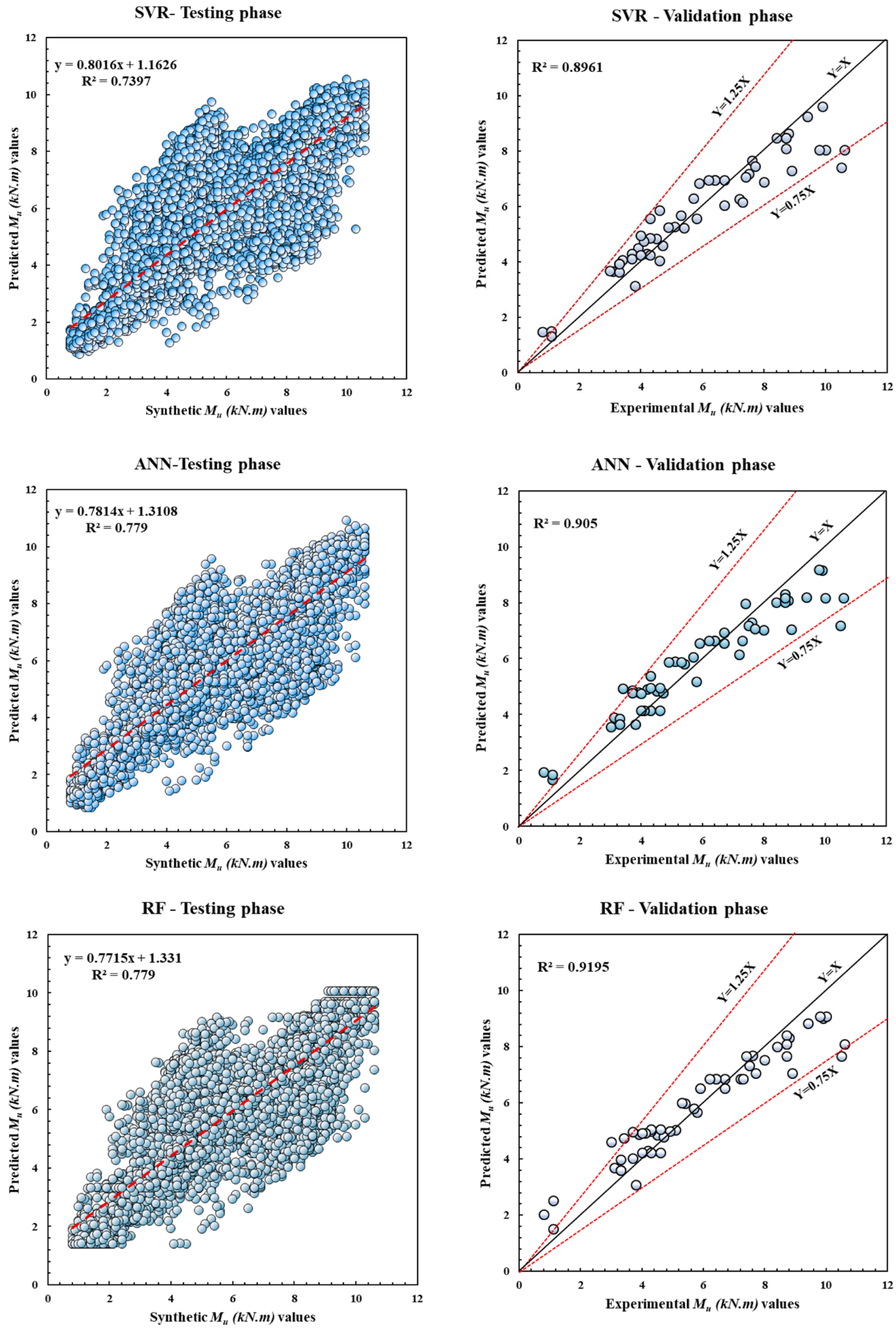

Fig. 9. Scatter plots of the proposed ML & EL models during the testing and validation phases for the cold-formed steel tubes.

To identify the best-fitting distribution for all the used variables (i.e. *t, d*, f_y, *E*, and M_u), the KS-test is utilized to explore five candidate distributions (i.e. Normal, Lognormal, Weibull, Gumbel, and Frechet). For each distribution, the KS-test is computed, and a corresponding *p-value* is obtained. The null hypothesis (H_0) assumes that the data follows the given theoretical distribution, while the alternative hypothesis (H_1) suggests that the data does not follow the given distribution. Thereafter, the best fitting distribution is selected based on the lowest KS-test value, as the value signifies a smaller deviation between the empirical and theoretical distributions.

Table 3 and Table 4 present the KS-test results for the fabricated and cold-formed steel tubes, respectively. The tables report the KS-test for each input and output variables across the tested distribution. The results illustrates that the Frechet distribution provides the best fit for all variables in cold-formed steel tubes, except of the output variable, where the Gumbel distribution yielded the lowest KS-test value. For fabricated steel tubes, the Frechet distribution exhibited the best fit for *t (mm)* and *d (mm)*, while the Weibull distribution was the most suitable for f_y *(MPa)* and M_u. In the case of *E (MPa)*, the *lognormal* distribution was identified as the best fit-distribution.

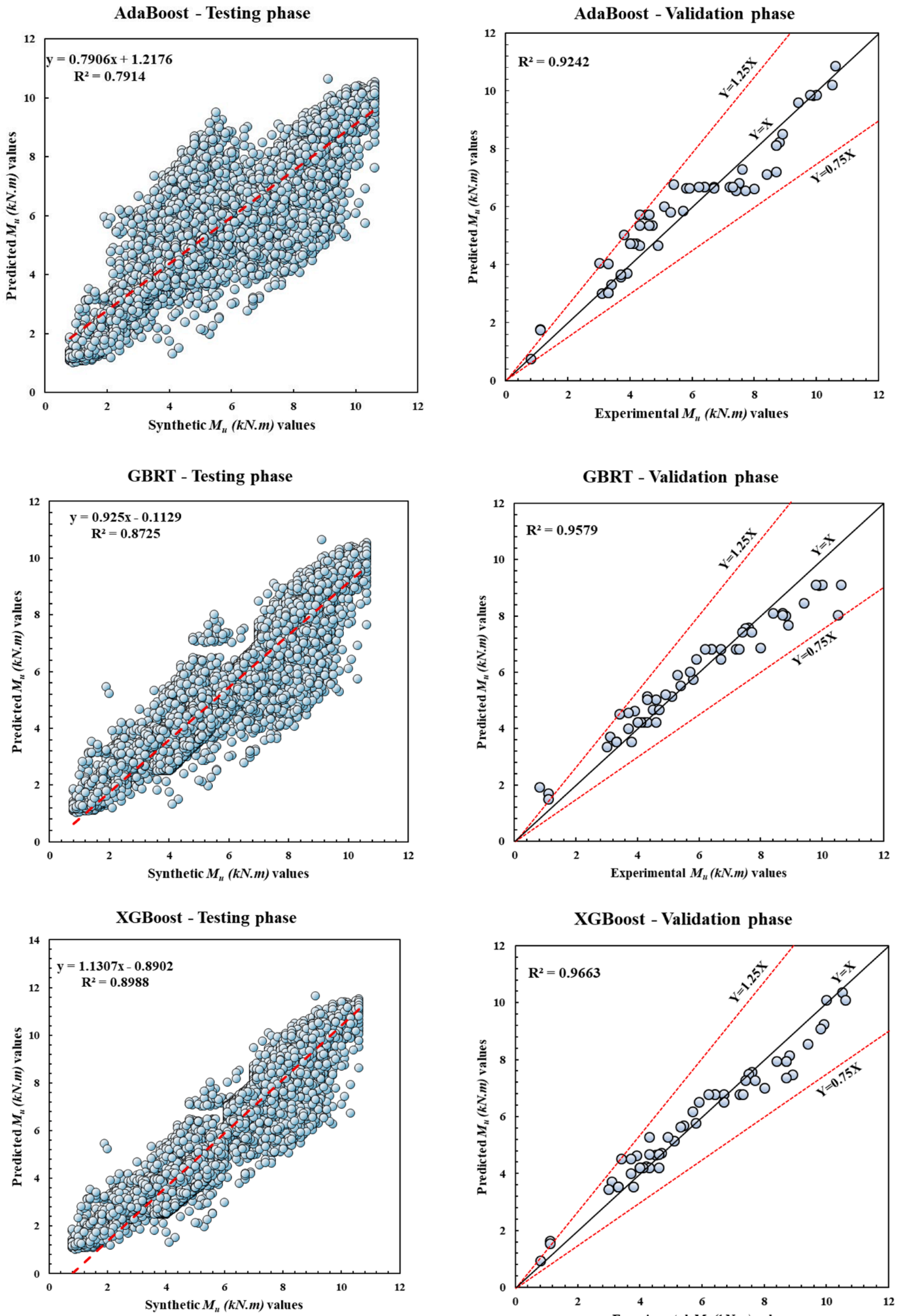

Fig. 9. (*continued*).

3.3. Statistical evaluation metrics

To ensure the accuracy of the deep generative based EL & ML models for the M_u prediction in CSTs, different statistical evaluation metrics are utilized. This latter compares the generated databases of the fabricated and cold-formed steel tubes with the predicted values of M_u using the EL & ML models, which will provide insights into the models' performance accuracy. Eleven statistical evaluation metrics comprising seven single and four global metrics are utilized in this study [65,66]. Furthermore, graphical metrics such as scatterplots and error histograms will be used to depict the proposed framework's agreement and effectiveness. The corresponding formulas and descriptions of these metrics are reported in Table 5.

4. Results and discussion

This section analyzes and discusses the results of the proposed framework in this study, starting by assessing the validity of the generated synthetic data for both fabricated and cold-formed steel tubes. Thereafter, the performance of the proposed ML-models (i.e. ANN and SVR) and El-models (i.e. RF, AdaBoost, GBRT, and XGBoost) is evaluated using the single and global statistical metrics and graphical illustrations based on the obtained results in the training, testing and validation phases. Finally, using the best performing model for predicting the UBC

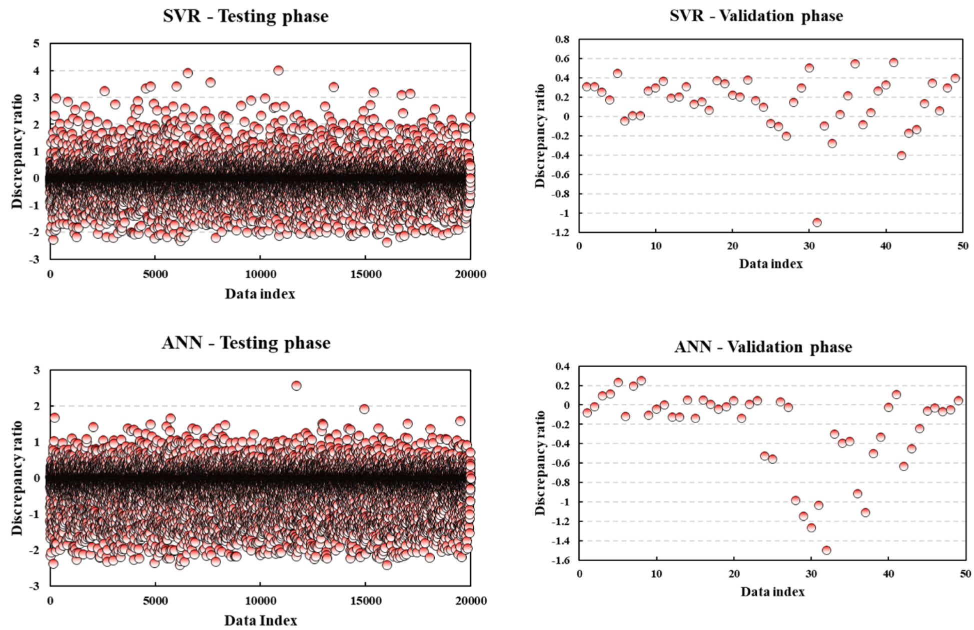

Fig. 10. DR-plots of the proposed ML & EL models during the testing and validation phases for the fabricated steel tubes.

of CSTs, SHAP analysis is performed, while results are discussed.

4.1. Synthetic data generation and evaluation

After running the CopulaGAN code with numerous different variables and adjustments (e.g. trial and error method) to establish the best performing process, an excellent replication of the original database is achieved using 1000 epochs, where 100,000 synthetic datasets were generated for each of the fabricated and cold-formed steel tubes. Then statistically evaluated against the original data in order to assess their credibility for further use in the modeling process. Table 6 and Table 7 present comparative statistics of the original and synthetic datasets for the fabricated and cold-formed steel tubes, respectively in terms of the minimum (**MIN**), maximum (**MAX**), quartiles (i.e. **Q1**: 25 % quartile; **Q2**: 50 % quartile and **Q3**: 75 % quartile), mean (**MEAN**) and standard deviation (**SD**) for each variable based on the relative error ($R_e = \frac{X_{org} - X_{syn}}{X_{org}}$; where, X_{org} represents the original value, and X_{syn} denotes the synthetic value). Positive R_e values signify under-generated synthetic data, while negative values present over-generated data. From the observed results in the tables, the generated synthetic data falls within the exact same range as the original range of the experimental data as the maximum and minimum values of the all the input and output variables for both fabricated and cold-formed steel tubes indicate $R_e = 0\,\%$. It can be noted that the majority of the comparative statistics indicated in Table 6 for all the variables have a $R_e < 10$ %, demonstrating high resemblance between the original and synthetic databases. However, higher R_e values can be identified for M_u that's ranging between −15 % and −33 %. Table 7 displays great replication of the original based on the synthetic database for the cold-formed steel tubes, as almost all the R_e values are lower than 10 %, except for 3 instances where the highest spotted R_e value is 19.82 %. The reported results in these tables show robust and reliable synthetic data that can be further used to train the ML & EL models. Both synthetic datasets accurately reproduce the original data, preserving variable ranges and distribution patterns as illustrated in Fig. 5 and Fig. 6, which display each variable's distribution based histogram for both the original and synthetic data, visualizing comparative patterns. Fig. 5 plots the histograms of the fabricated circular steel tubes, while Fig. 6 illustrates the histograms of the cold-formed circular steel tubes. The graphical comparative analysis of the original and synthetic data distributions reveals strong similarities for almost all variables, suggesting preserved statistical properties. Both synthetic datasets for the fabricated and cold-formed steel tubes effectively replicate the original data, maintaining consistency in variable ranges and distribution patterns. This strong consistency ensures the synthetic datasets can serve as a credible and accurate substitute for the original in the next steps.

4.2. Performance evaluation of the ML & EL models

To attain the objective of establishing robust and reliable ML & EL models for predicting the UBC of CSTs (i.e. Fabricated and cold-formed steel tubes), the developed models were evaluated and ranked based on their performances during the training (i.e. 80 % of the synthetic datasets), testing (i.e. 20 % of the synthetic datasets) and validation (i.e. original experimental datasets) phases. The evaluation procedure of the proposed ML (i.e. ANN & SVR) and EL (i.e. RF, AdaBoost, GBRT & XGBoost) models is conducted in a systematic order, commencing with the single metrics, then the global metrics, followed by comparative graphical illustration.

Table 8 and Table 9 display the comparative performance evaluation results of the ML & EL models based on the single statistical metrics (i.e. RMSE, MAPE, MAE, NSE, and WI) during the training, testing, and validation phases for the fabricated and cold-formed steel tubes, respectively. The model with the best performance is the one exhibiting the lowest RMSE, MAPE, and MAE values and the highest NSE, and WI values.

It was found that all ML & EL models reveal acceptable results with varied performances. It can be seen from both tables that training phase results are higher than the testing phase, which is reasonable as 80 % of the synthetic data was fed to the ML & EL models (both input and output) to build the models, meanwhile 20 % of the synthetic data was given to test the ML & EL models, giving the models only the input variables. On the other hand, the validation phase gives higher results than the training and testing phases, demonstrating the predictive capability of the proposed models for accurate predictions of M_u in small database. According to both tables, the XGBoost demonstrated the best results based on the majority of the metrics for training, testing, and validation phases. From Table 8, XGBoost yielded the lowest RMSE

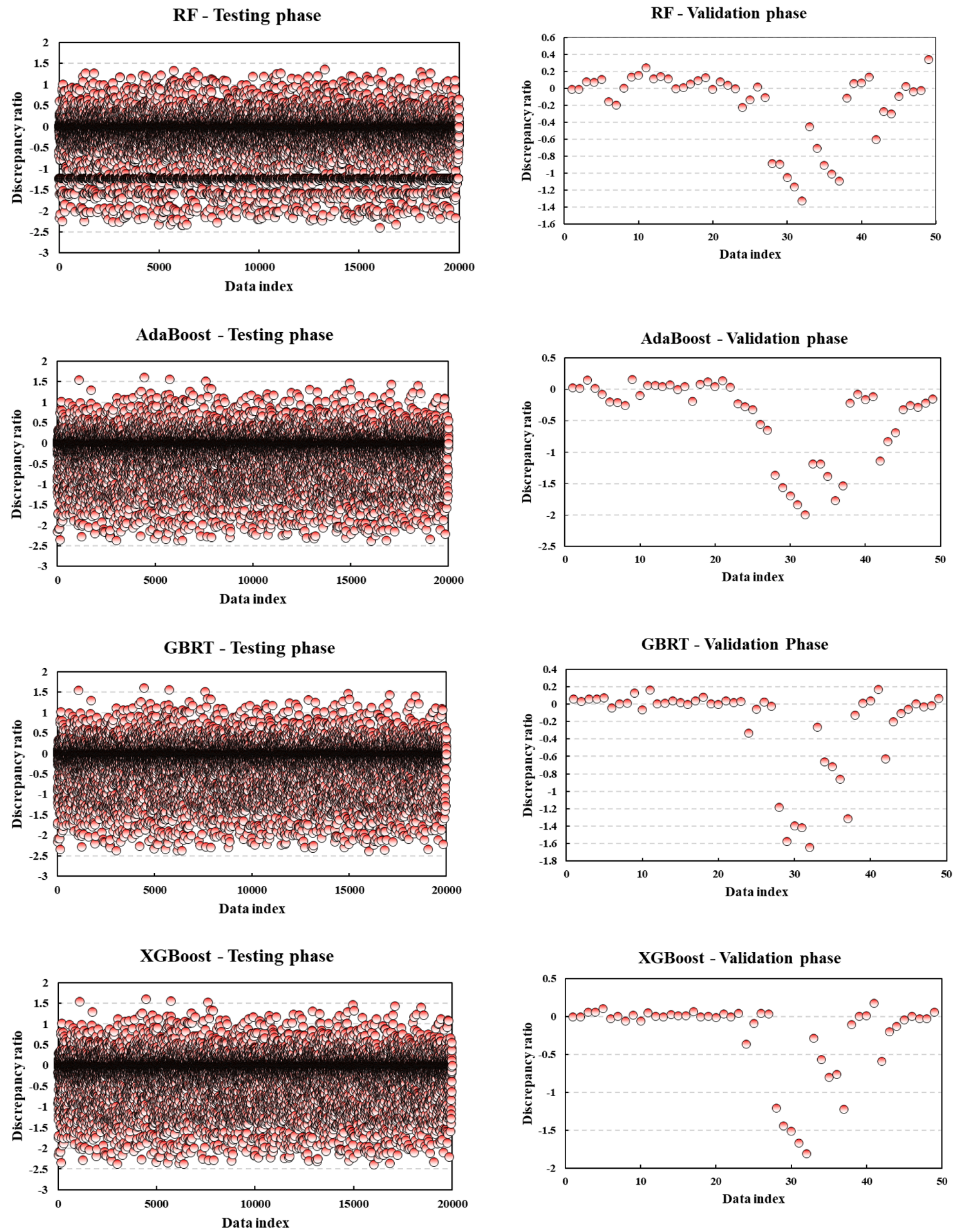

Fig. 10. (*continued*).

values ($RMSE^{Training}$ =131.8125 kN.m, $RMSE^{Testing}$ = 157.7568 kN.m, $RMSE^{Validation}$ = 77.9627 kN.m) and the highest WI values ($WI^{Training}$ = 98.53 %, $WI^{Testing}$ = 97.87 %, $WI^{Validation}$ = 99.51 %). However, MAPE indicates that the SVR shows the lowest values, ($MAPE^{Training}$ = 202.1951 %, $MAPE^{Testing}$ = 186.3033 %, $MAPE^{Validation}$ = 64.8882 %). Similar observations are noted from Table 9, where XGBoost scored the lowest RMSE values ($RMSE^{Training}$ =0.6890 kN.m, $RMSE^{Testing}$ = 0.8646 kN.m, $RMSE^{Validation}$ = 0.5402 kN.m) and the highest WI values ($WI^{Training}$ = 97.67 %, $WI^{Testing}$ = 96.50 %, $WI^{Validation}$ = 98.61 %). Only two metrics indicated better values using AdaBoost during the testing phase: MAPE = 11.8732 % and MAE = 0.6309 kN.m. Based on the validation phase results, the XGBoost model improved GBRT, AdaBoost, RF, ANN, and SVR by 70,29 %, 157,60 %, 150,36 %, 155,03 %, and 386,69 % for the fabricated steel tubes and 24,26 %, 32,78 %, 59,03 %, 71,41 %, and 63,23 % for cold-formed steel tubes, in term of RMSE, respectively. However, as different single metrics delivered varied results, it is necessary to use global metrics to evaluate and rank the proposed ML & EL models' performances.

Fig. 7(a) and (b) illustrate the global metrics results in term of a bar chart for the fabricated and cold-formed steel tubes using the proposed ML & EL models, respectively. According to the obtained PI results, the models' performance are ranked as XGBoost > AdaBoost > GRBT > RF > ANN > SVR for fabricated steel tubes, and XGBoost > GBRT > AdaBoost > RF > ANN > SVR for cold-formed steel tubes, where XGBoost reports the lowest value ($PI^{fabricated}$ = 0.7979, $PI^{cold\text{-}formed}$ = 0.8176). On the other hand, SVR indicate a low performance compared to the other proposed models for both fabricated and cold-formed steel tubes, exhibiting the highest OBJ value ($OBJ^{fabricated}$ = 417.0443, $OBJ^{cold\text{-}formed}$ = 0.8176) and the lowest CI scores ($CI^{fabricated}$ = 0.8019, $CI^{cold\text{-}formed}$ = 0.6810). Using R_e between the PI values of the ML & EL models reveals that the XGBoost model outperforms the GBRT, AdaBoost, RF, ANN and SVR models by 2.91 %, 2.18 %, 12.65 %, 16.43 %, and 17.32 % for fabricated steel tubes and 5.11 %, 5.64 %, 13.36 %, 16.01 %, and 22.31 %, for cold-formed tubes, respectively.

Fig. 8 and Fig. 9 illustrate the scatterplots during the testing and validation phases using the predicted and synthetic/experimental values

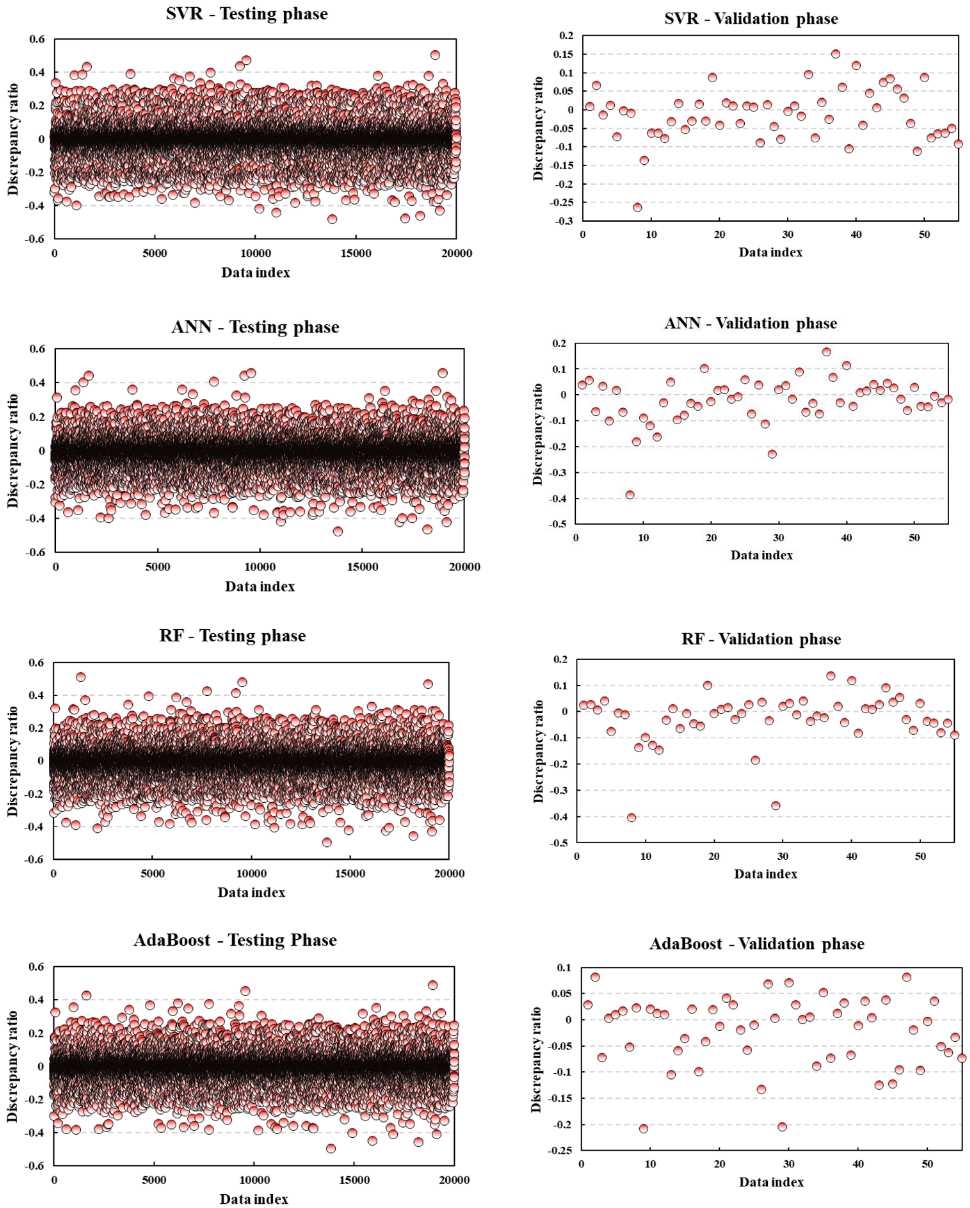

Fig. 11. DR-plots of the proposed ML & EL models during the testing and validation phases for the cold-formed steel tubes.

of M_u based on the ML & EL models for the fabricated and cold-formed steel tubes, respectively. In the testing phase plots, the red dashed line represents the regression-line between the predicted and synthetic data formulated by the function $\boldsymbol{Y} = a\boldsymbol{X}+b$ ($a = 1$ and $b = 0$ represent a perfect agreement between the predicted and synthetic data). In the validation phase, the black line represents a perfect agreement between the predicted and experimental values of M_u ($\mathbf{Y} = \mathbf{X}$), while the red dotted lines depict margin agreement errors of ±25 %. All scatterplots comprise their corresponding R^2 values.

From the R^2 values reported in the figures the overall agreements between the predicted and synthetic data are acceptable, where $R^2 \in$ [0.8431 , 0.9210] for fabricated steel tubes and $R^2 \in$ [0.7397,0.8988] for the cold-formed steel tubes in the testing phase. On the other side, a higher agreement can be observed in the validation phase as $R^2 \in$ [0.9094, 0.9853] for fabricated steel tubes and $R^2 \in$ [0.8961,0.9663] for cold-formed steel tubes, confirming similar remarks as in Table 1 and Table 2. Fig. 8 indicates that the majority of the validation predictions fall within the ±25 % error margins, however the models show relatively higher error for small M_u values, which can be returned to the fact that the fabricates steel tubes have a large range of M_u values ($M_u \in$ [1.6, 1892.7]). All the validation predictions reported in Fig. 9 are withing the ±25 % error margins, noting that M_u values for the cold-formed steel tubes range between 0.8 kN.m to 10.6 kN.m.

Among the proposed ML & EL models, XGBoost reveals the highest agreement for both fabricated steel tubes ($R^2_{testing}$ = 0.9210 and $R^2_{validation}$= 0.9853) and cold-formed steel tubes ($R^2_{testing}$ = 0.8988 and $R^2_{validation}$= 0.9663). Contrarily, SVR demonstrates the lowest agreement with $R^2_{testing}$ = 0.8431 and $R^2_{validation}$= 0.9094 for fabricated steel tubes and $R^2_{testing}$ = 0.7397 and $R^2_{validation}$= 0.8961 for cold-formed steel tubes. Finally, based on the validation results, XGBoost improved the prediction results compared to GBRT, AdaBoost, RF, ANN, and SVR by 1.97 %, 4.23 %, 5.30 %, 6.10 %, and 7,10 % for fabricated steel tubes, and 0.87 %, 4.36 %, 4.84 %, 6.34 %, and 7.26 % for cold-formed steel tubes, respectively.

DR-plots is another graphical illustration used to evaluate the

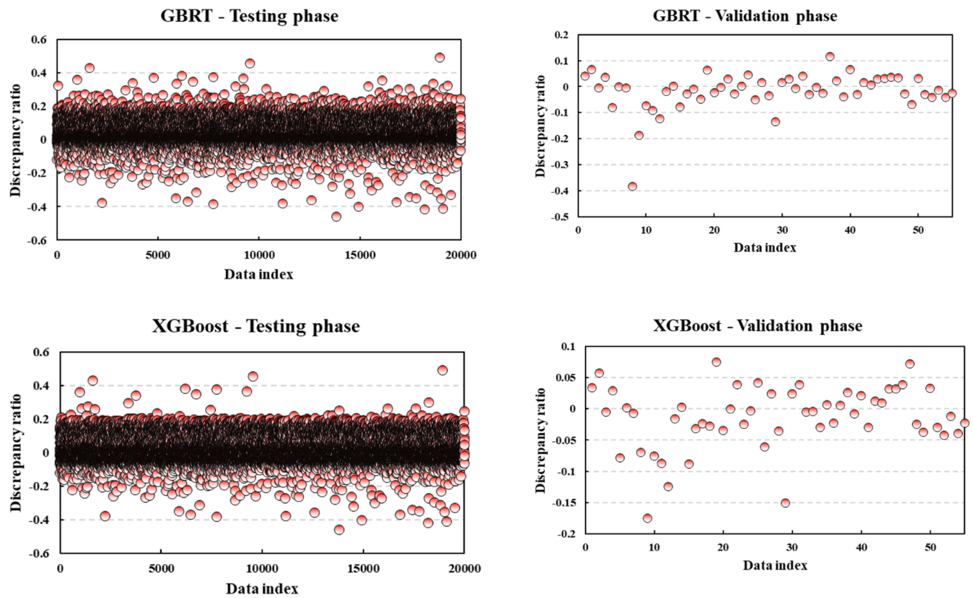

Fig. 11. (*continued*).

models' performances. This graphical metric indicates the degree of uncertainty in the model as it demonstrates the deviation, where the closer the DR values are to zero, the higher accuracy the model is. Positive values indicate overprediction, while negatives values imply underprediction. Fig. 10 and Fig. 11 highlight the DR-plots for the fabricated and cold-formed steel tubes during the testing and validation phases based on the provided results from the ML & EL models.

It can be seen that the proposed models show low overall uncertainties, as most of the DR values revolve approximately around zero for both fabricated and cold-formed steel tubes in both phases. Although the DR-plots show excellent overall results; it can be observed from Fig. 10 that the ML & EL models slightly tend to underpredict the M_u small values for fabricates steel tubes. The ML & EL models exhibit different uncertainty levels, based on the DR values, where SVR indicates the highest uncertainties for fabricates steel tubes (testing: [−2.3842, 3.9968] and validation: [−1.8124, 0.5622]), and RF for cold-formed tubes (testing: [−0.4990, 0.5089] and validation: [−0.4048, 0.1362]). The lowest uncertainties were provided by XGBoost during the testing (fabricated steel tubes: [−1.8124, 0.1744] and cold-formed steel tubes: [−0.4589, 0.4903]) and validation (fabricated steel tubes: [−2.3872, 1.6063] and cold-formed steel tubes: [−0.1748, 0.0755]) phases. These results demonstrate the accuracy of the XGBoost model, compared to the other proposed models for UBC modeling in CSTs.

Finally, Taylor diagram is utilized as a global graphical comparative illustration, combining three metrics: coefficient of correlation, standard deviation [SD], and RMSE to further evaluate the models' performances. The robustness of the proposed predictive ML & EL models is illustrated by the closeness to the experimental data, anointed as red square in the diagrams, where the closer the model is, the better its predictive capabilities are. The SD values are represented by the dashed circles that center from the origin, whereas the correlation coefficient values are the dotted circles that centers from the experimental M_u value. Fig. 12 summarizes the Taylor diagrams for the fabricated and cold-formed steel tubes based on the validation phase results. According to the visual results observed from the Taylor diagrams, XGBoost is the closest model to the experimental data for both fabricated and cold-formed steel tubes, with a correlation of coefficient of 0.993 and 0.983; and a total SD of 542.91 kN.m and 2.12 kN.m, in same respect. Thus, the XGBoost model exhibits excellent results expressing robust and reliable accuracy for predicting UBC of CSTs based on all metrics and results. Furthermore, both figures reveals GBRT as the second closest model, indicating great robustness and predictability.

4.3. XGBoost based SHAP analysis

Using the best-performing model, XGBoost, SHAP analysis based model explainability is conducted to illustrate the output decision-making process. Starting by local explainability/interpretability, the SHAP force plots using the XGBoost model for sample [$X = 2$] are provided in Fig. 13(a) and (b) for fabricated and cold-formed steel tubes, respectively. This type of figures visually illustrates how the model (i.e. XGBoost) reached its decision regarding sample 2 using an additive force configuration. This latter comprises red and blue bar arrows, with the first indicating the variables that increase the prediction values and the second indicating the variables that lower them, all leading towards the final sample output $f(X = 2)$.

According to the SHAP force plots in Fig. 13(a) for fabricated steel tubes, the final outcome $f(X = 2) = 539.02$ *kN.m*. The figure demonstrates that the decision based XGBoost model used to achieve this final output incorporated the values of three variables; the diameter ($d = 458$ *mm*), yield strength ($f_y = 434$ *MPa*), and modulus of elasticity ($E = 199.501$ *MPa*) to increase toward the final output and one value (while thickness, $t = 6.8$ *mm*) to decrease towards the final output. Similarly, for cold-formed steel tubes, Fig. 13(b) indicates that the final output $f(X = 2) = 5.82$ *kN.m* is achieved based on the decision of using the values of two variables to increase the prediction towards the final outcome, the thickness ($t = 2.45$ *mm*) and modulus of elasticity ($E = 217.1$ *MPa*), and the values two variables, yield strength ($f_y = 415$ *MPa*) and diameter ($d = 76.3$ *mm*), to decrease the prediction towards the final outcome.

In contrast to the SHAP force plot based on the local explanation, Figs. 14 and 15 provide the global explanation for fabricated and cold-formed steel tubes, respectively, using (a) the global feature importance bar plot and (b) the beeswarm summary plot. The first plot (-a- global feature importance bar) shows the global importance of each variable in the decision-making-based XGBoost model towards the final outcomes, computed using the mean absolute SHAP values of all experimental samples. The second plot (-b- beeswarm summary plot) shows the global explanation for each variable using all SHAP values from each sample separately. For each variable, the SHAP value for each sample is represented by a single dot (red = high, blue = low), which accumulates horizontally to indicate the density and likelihood of impact on the model output.

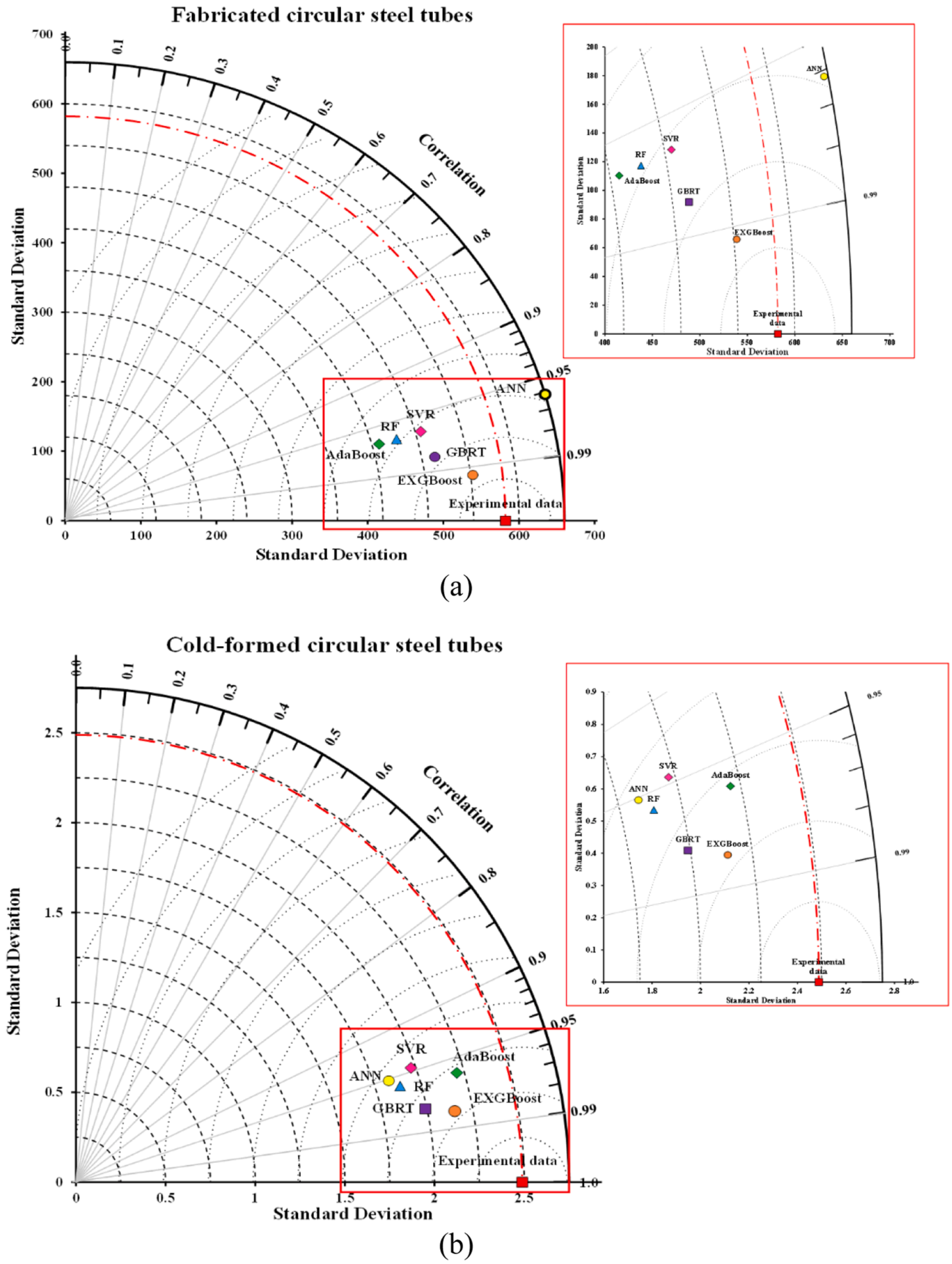

Fig. 12. Taylor diagram summary of proposed ML & EL models based on the validation results. (a) fabricated steel tubes and (b) cold-form steel tubes.

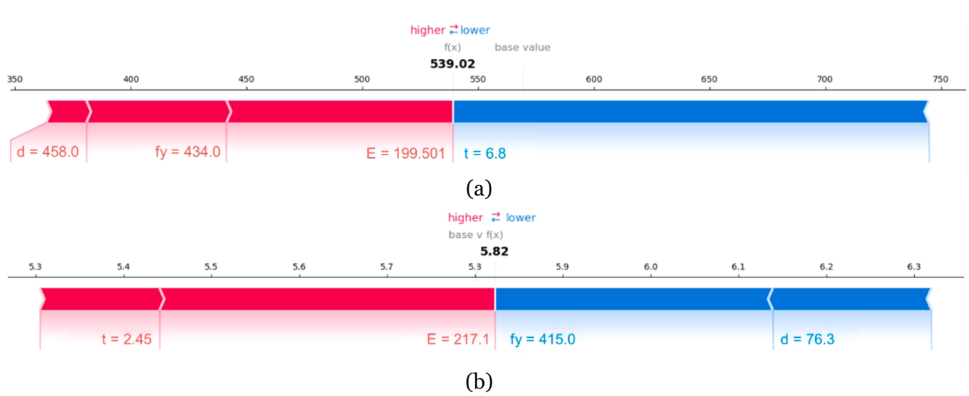

Fig. 13. SHAP force plots based on XGBoost model. (a) Fabricated steel tubes, and (b) cold-formed tubes.

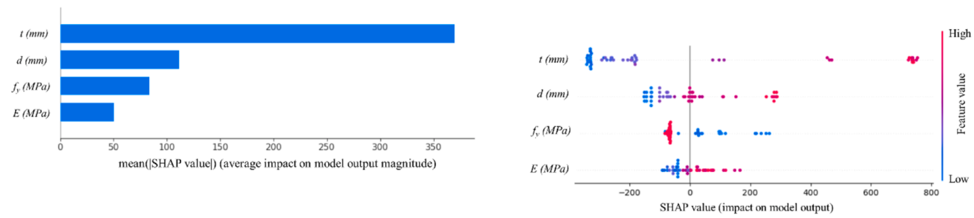

(a) (b)

Fig. 14. SHAP plots based on XGBoost model for fabricated steel tubes. (a) Global feature importance bar plot, and (b) Beeswarm summary plot.

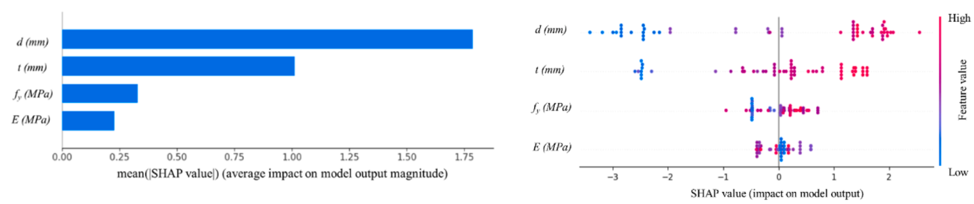

(a) (b)

Fig. 15. SHAP plots based on XGBoost for cold-formed steel tubes. (a) Global feature importance bar plot, and (b) Beeswarm summary plot.

According to the results of the global feature importance bar plot, *t* has the highest impact on M_u predictions, followed by *d*, for fabricated steel tubes, while it can be seen the opposite for the cold-formed steel tubes, with *t* has the highest impact on M_u predictions, followed by *t*. The remaining variables (f_y and *E*) have the same order and relevance in modeling M_u. These findings are consistent with the statistical analysis-based Pearson correlation performed earlier for the experimental datasets. SHAP beeswarm plots provide in depth explanation regarding the variables' influence on M_u predictions. In Fig. 14(b), *t* appear as the variables with the highest impact, with larger values contributing to increasing predictions. In contrast, *E* has minimal influence, with dense SHAP values near zero. Interestingly, f_y has a negative correlation with the output, indicating that lower values contribute more significantly to prediction gains. Fig. 15(b) indicates that higher values of *d* correspond positively to M_u predictions, while *t* follows the same pattern, and both f_y and *E* have a minimal impact with dense SHAP values around zero.

5. Conclusion

This paper introduces a novel two-stage framework for deep generative based ML & EL modeling of ultimate bending capacity in circular steel tubes. The first stage involves using the Copula Generative Adversarial Network with limited experimental datasets of fabricated and cold-formed circular tubes to reproduce an accurate large synthetic database that replicates the original databases. After that, two ML models (ANN and SVR) and four EL models (RF, AdaBoost, GBRT, and XGBoost) were trained and tested using the synthetic database. The developed ML & EL models were then validated using the original databases. The performance of the outcome ML & EL models is then assessed using various metrics and ranked, with the best performing model explained using SHAP analysis. The following conclusions can be taken from this research:

1. The proposed CopulaGAN framework accurately generated large databases of 100,000 datasets that replicate the original databases based on only 49 for fabricated circular steel tubes and 55 cold-formed circular steel tubes. This is confirmed by the R_e values of all used variables (Min-Max: $Re = 0$ %) and the similarity of data distribution between the synthetic - experimental datasets.
2. Based on the results obtained by the performance metrics during the training and testing phases using the synthetic datastes and validated using the original datasets, all the proposed ML & EL models yielded acceptable results with varied performances. The lowest performance among the proposed models (i.e. SVR) indicates $R^2 = 0.9094$ and $R^2 = 0.8991$ and RMSE of 77.9627 kN.m and 0.5402 kN.m for fabricated and cold-formed steel tubes, respectively.
3. The XGBoost achieved superior performances compared to all the ML & EL models during all phases and based on all comparative metrics. Using the global metric PI, the XGBoost model outperforms the GBRT, AdaBoost, RF, ANN and SVR models by 2.91 %, 2.18 %, 12.65 %, 16.43 %, and 17.32 % for fabricated steel tubes and 5.11 %, 5.64 %, 13.36 %, 16.01 %, and 22.31 %, for cold-formed tubes, respectively.
4. The graphical illustrations visually demonstrated the accuracy of the XGBoost model, where it produced the lowest uncertainties during the modelling process (fabricated steel tubes: [−2.3872, 1.6063] and cold-formed steel tubes: [−0.1748, 0.0755]) while it shows the closest agreement with the experimental data based on the Taylor diagram.
5. The SHAP analysis based XGBoost model revealed that *t* is the most influential variable for M_u modeling followed by the diameter for fabricated steel tubes, whereas *d* identified as the most impactful variable on M_u modeling for cold-formed steel tubes, followed by *t*. These results confirm the statistical analysis conducted on the experimental dataset.

CRediT authorship contribution statement

Mahmood Sami Salah: Writing – original draft, Visualization, Software, Methodology, Formal analysis, Conceptualization. **Mohamed El Amine Ben Seghier:** Writing – original draft, Visualization, Software, Methodology, Formal analysis, Investigation, Conceptualization, Project administration. **Sushant Gautam:** Writing – original draft, Validation, Software, Investigation. **Osama Ahmed Mohamed:** Writing – original draft, Validation, Resources, Funding acquisition.

Declaration of competing interest

The authors declare that they have no known competing financial interests or personal relationships that could have appeared to influence the work reported in this paper.

Acknowledgements

The authors' acknowledge the funded APC by Oslo Metropolitan University. The second author also thanks the support of the Van Lang University.

Data availability

Data will be made available on request.

References

[1] W. Zhang, S. Chen, Y. Zhu, et al., Experimental study on the axial compression behavior of circular steel tube short columns under coastal environmental corrosion, Thin-Walled Struct. 200 (2024) 111929.
[2] L. Han, W. Li, R. Bjorhovde, Developments and advanced applications of concrete-fi lled steel tubular (CFST) structures : members Concrete cracks, JCSR 100 (2014) 211–228, https://doi.org/10.1016/j.jcsr.2014.04.016.
[3] M. Elchalakani, X.L. Zhao, R.H. Grzebieta, Plastic mechanism analysis of circular tubes under pure bending, Int. J. Mech. Sci. 44 (2002) 1117–1143.
[4] J.F. Hajjar, Concrete-filled steel tube columns under earthquake loads, Prog. Struct. Eng. Mater. 2 (2000) 72–81.
[5] F.C. Bardi, S. Kyriakides, Plastic buckling of circular tubes under axial compression—part I: experiments, Int. J. Mech. Sci. 48 (2006) 830–841.
[6] Elchalakani M., Zhao X.L., Grzebieta R.H. (2001) Concrete-filled circular steel tubes subjected to pure bending. 57:1141–1168.
[7] W. Ma, Z. Sun, H. Wu, et al., Buckling analysis of thin-walled circular shells under local axial compression using vector form intrinsic finite element method, Metals 13 (2023) 564.
[8] Structures C-FS (2005) Standards Australia/Standards New Zealand. Wellington, New Zeal.
[9] (2016) Standards Association of Australia, As 4100-1998 steel structures.
[10] A. Committee, Specification For Structural Steel Buildings (ANSI/AISC 360-10), American Institute of Steel Construction, Chicago-Illinois, 2010.
[11] P. Code, Eurocode 3: Design of Steel Structures-Part 1-2: General rules-Structural Fire Design, London Eur Comm Stand, 2007.
[12] X. Qiu, X. Yu, Y. Li, T.X. Yu, The deformation mechanism analysis of a circular tube under free inversion, Thin-Walled Struct. 107 (2016) 49–56.
[13] S.R. Reid, Plastic deformation mechanisms in axially compressed metal tubes used as impact energy absorbers, Int. J. Mech. Sci. 35 (1993) 1035–1052.
[14] Y. Chen, J. Zhang, H. Zhang, et al., Ultimate bending capacity of strain hardening steel pipes, China Ocean Eng. 30 (2016) 231–241.
[15] A.B. Knupp, M.A. Vaz, J.C.R. Cyrino, Ultimate bending capacity of perforated pipe cross sections, Mar. Syst. Ocean Technol. 14 (2019) 34–41.
[16] F. Hartmann, C. Katz, Structural Analysis with Finite Elements, Springer Science & Business Media, 2004.
[17] L. Han, G.-H. Yao, Z. Tao, Performance of concrete-filled thin-walled steel tubes under pure torsion, Thin-walled Struct. 45 (2007) 24–36.
[18] R. Wang, L. Han, C.-C. Hou, Behavior of concrete filled steel tubular (CFST) members under lateral impact: experiment and FEA model, J. Constr. Steel. Res. 80 (2013) 188–201.
[19] Zhang Z., Zhong Y. (2021) A FEA method for mathematical calculation and prediction analysis cross-sectional ovalization of tubes under rotary straightening. In: Journal of Physics: Conference Series. IOP Publishing, p 42057.
[20] P. Lu, S. Chen, Y. Zheng, Artificial intelligence in civil engineering, Math. Probl. Eng. 2012 (2012) 145974.
[21] M.E.A. Ben Seghier, E.M. Golafshani, J. Jafari-Asl, M. Arashpour, Metaheuristic-based machine learning modeling of the compressive strength of concrete containing waste glass, Struct. Concr. (2023).
[22] Y. Huang, J. Fu, Review on application of artificial intelligence in civil engineering, Comput. Model. Eng. Sci. 121 (2019) 845–875.
[23] M.E.A. Ben Seghier, Elshaboury N, E.M. Abdelkader, et al., Two-stage framework for lateral-torsional buckling resistance prediction of cellular steel beams under fire conditions. Structures, Elsevier, 2024 107157.
[24] M.E.A. Ben Seghier, O.A. Mohamed, H. Ouaer, Machine learning-based Shapley additive explanations approach for corroded pipeline failure mode identification. Structures, Elsevier, 2024 106653.
[25] B. Manzoor, I. Othman, S. Durdyev, et al., Influence of artificial intelligence in civil engineering toward sustainable development—a systematic literature review, Appl. Syst. Innov. 4 (2021) 52.
[26] M. Alfouneh, S.M. Ben, B. Keshtegar, S.A.T. Shojah, A new formulation for predicting the ultimate capacities of FRP-confined concrete using advanced machine learning framework: developed structural reliability analysis, Structures (2024) 107158.
[27] Y. Xu, B. Zheng, M. Zhang, Capacity prediction of cold-formed stainless steel tubular columns using machine learning methods, J. Constr. Steel. Res. 182 (2021) 106682.
[28] H. Basarir, M. Elchalakani, A. Karrech, The prediction of ultimate pure bending moment of concrete-filled steel tubes by adaptive neuro-fuzzy inference system (ANFIS), Neural Comput. Appl. 31 (2019) 1239–1252.
[29] M. Shahin, M. Elchalakani, Neural networks for modelling ultimate pure bending of steel circular tubes, J. Constr. Steel. Res. 64 (2008) 624–633.
[30] L. Simwanda, P. Gatheeshgar, F.M. Ilunga, et al., Explainable machine learning models for predicting the ultimate bending capacity of slotted perforated cold-formed steel beams under distortional buckling, Thin-Walled Struct. 205 (2024) 112587.
[31] M.E.A. Ben Seghier, V. Plevris, G. Solorzano, Random forest-based algorithms for accurate evaluation of ultimate bending capacity of steel tubes. Structures, Elsevier, 2022, pp. 261–273.
[32] I.J. Goodfellow, J. Pouget-Abadie, M. Mirza, et al., Generative adversarial nets, Adv. Neural Inf. Process. Syst. 27 (2014).
[33] A. Creswell, T. White, V. Dumoulin, et al., Generative adversarial networks: an overview, IEEe Signal. Process. Mag. 35 (2018) 53–65.
[34] I. Goodfellow, J. Pouget-Abadie, M. Mirza, et al., Generative adversarial networks, Commun. ACM 63 (2020) 139–144.
[35] L. Xu, M. Skoularidou, A. Cuesta-Infante, K. Veeramachaneni, Modeling tabular data using conditional gan, Adv. Neural Inf. Process. Syst. 32 (2019).
[36] N. Patki, R. Wedge, K. Veeramachaneni, The synthetic data vault, in: 2016 IEEE International Conference on Data Science and Advanced Analytics (DSAA), IEEE, 2016, pp. 399–410.
[37] H.-T. Thai, Machine learning for structural engineering: a state-of-the-art review. Structures, Elsevier, 2022, pp. 448–491.
[38] A.T.G. Tapeh, M.Z. Naser, Artificial intelligence, machine learning, and deep learning in structural engineering: a scientometrics review of trends and best practices, Arch. Comput. Methods Eng. 30 (2023) 115–159.
[39] H. Adeli, Neural networks in civil engineering: 1989–2000, Comput. Civ. Infrastruct. Eng. 16 (2001) 126–142.
[40] M.E.A. Ben Seghier, B. Kechtegar, M.N. Amar, et al., Simulation of the ultimate conditions of fibre-reinforced polymer confined concrete using hybrid intelligence models, Eng. Fail. Anal. 128 (2021) 105605.
[41] A. Çevik, A.E. Kurtoğlu, M. Bilgehan, et al., Support vector machines in structural engineering: a review, J. Civ. Eng. Manag. 21 (2015) 261–281.
[42] A.J. Smola, B. Schölkopf, A tutorial on support vector regression, Stat. Comput. 14 (2004) 199–222.
[43] M. Awad, R. Khanna, M. Awad, R. Khanna, Support vector regression, Effic. Learn. Mach. Theor. Concepts Appl. Eng. Syst. Des. (2015) 67–80.
[44] F. Zhang, L.J. O'Donnell, Support vector regression. Machine Learning, Elsevier, 2020, pp. 123–140.
[45] B.L. Random, For. Mach. Learn. 45 (2001) 5–32.
[46] D. Feng, W.-J. Wang, S. Mangalathu, et al., Implementing ensemble learning methods to predict the shear strength of RC deep beams with/without web reinforcements, Eng. Struct. 235 (2021) 111979.
[47] Z.-H. Zhou, Ensemble learning. Machine Learning, Springer, 2021, pp. 181–210.
[48] Y. Freund, R. Schapire, N. Abe, A short introduction to boosting, J.-Jpn. Soc. Artif. Intell. 14 (1999) 1612.
[49] C. Ying, M. Qi-Guang, L. Jia-Chen, G. Lin, Advance and prospects of AdaBoost algorithm, Acta Autom. Sin. 39 (2013) 745–758.
[50] T.N. Rincy, R. Gupta, Ensemble learning techniques and its efficiency in machine learning: a survey, in: 2nd International Conference on Data, Engineering and Applications (IDEA), IEEE, 2020, pp. 1–6.
[51] Brownlee J.A. Gentle introduction to the gradient boosting algorithm for machine learning. 2016.
[52] C. Li, A gentle introduction to gradient boosting (2016). http//www.ccs.neu.du/home/vip/teach/MLcourse/4_Boost.pdf. URL.
[53] T. Chen, C. Guestrin, Xgboost: a scalable tree boosting system, in: Proceedings of the 22nd ACM SIGKDD International Conference on Knowledge Discovery and Data Mining, 2016, pp. 785–794.
[54] Z.A. Ali, Z.H. Abduljabbar, H.A. Tahir, et al., eXtreme gradient boosting algorithm with machine learning: a review, Acad. J. Nawroz Univ. 12 (2023) 320–334.
[55] A.J. Rios, M.E.A. Ben Seghier, V. Plevris, J. Dai, Explainable ensemble learning framework for estimating corrosion rate in suspension bridge main cables, Results. Eng. 23 (2024) 102723.
[56] D.R. Sherman, Inelastic flexural buckling of cylinders. Proceeding, Invited Papers for the International Conference, 1986, pp. 339–356.
[57] D.R. Sherman, Tests of circular steel tubes in bending, J. Struct. Div. 102 (1976) 2181–2195.
[58] C.G. Schilling, Buckling strength of circular tubes, J. Struct. Div. 91 (1965) 325–348.
[59] J.O. Jirsa, F.H. Lee, J.C. Wilhoit Jr, J.E. Merwin, Ovaling of pipelines under pure bending, in: Offshore Technology Conference, OTC, 1972. OTC-1569.
[60] R.M. Korol, J. Hudoba, Plastic behavior of hollow structural sections, J. Struct. Div. 98 (1972) 1007–1023.
[61] M. Elchalakani, X.L. Zhao, R.H. Grzebieta, Plastic slenderness limits for cold-formed circular hollow sections, Aust. J. Struct. Eng. 3 (2002) 127–141.
[62] M. Elchalakani, X.-L. Zhao, R. Grzebieta, Variable amplitude cyclic pure bending tests to determine fully ductile section slenderness limits for cold-formed CHS, Eng. Struct. 28 (2006) 1223–1235.
[63] Berger V.W., Zhou Y. (2014) Kolmogorov–smirnov test: overview. Wiley statsref Stat Ref online.

[64] G. Fasano, A. Franceschini, A multidimensional version of the Kolmogorov–Smirnov test, Mon. Not. R. Astron. Soc. 225 (1987) 155–170.
[65] M.E.A. Ben Seghier, T.T. Truong, C. Feiler, D. Höche, A hybrid deep learning model for predicting atmospheric corrosion in steel energy structures under maritime conditions based on time-series data, Results Eng. (2025) 104417.
[66] S.M. Ben, C. Hermes, C.C. de Faria, et al., Numerical analysis and prediction of lateral-torsional buckling resistance of cellular steel beams using FEM and least square support vector machine optimized by metaheuristic algorithms, Alex. Eng. J. 67 (2023) 489–502.